Mantle structure and flow across the continent-ocean transition of the eastern North American margin: anisotropic S-wave tomography

Brennan Brunsvik[1], Zachary Eilon[1], and Colton Lynner[2]

[1]University of California Santa Barbara
[2]University of Delaware

November 22, 2022

Abstract

Little has been seismically imaged through the lithosphere and mantle at rifted margins across the continent-ocean transition. A 2014-2015 community seismic experiment deployed broadband seismic instruments across the shoreline of the eastern North American rifted margin. Previous shear-wave splitting along the margin shows several perplexing patterns of anisotropy, and by proxy, mantle flow. Neither margin parallel offshore fast azimuths nor null splitting on the continental coast obviously accord with absolute plate motion, paleo-spreading, or rift-induced anisotropy. Splitting measurements, however, offer no depth constraints on anisotropy. Additionally, mantle structure has not yet been imaged in detail across the continent-ocean transition. We used teleseismic S, SKS, SKKS, and PKS splitting and differential travel times recorded on ocean-bottom seismometers, regional seismic networks, and EarthScope Transportable Array stations to conduct joint isotropic/anisotropic tomography across the margin. The velocity model reveals a transition from fast, thick, continental keel to low velocity, thinned lithosphere eastward. Imaged short wavelength velocity anomalies can be explained by edge-driven convection. We also find layered anisotropy. The anisotropic fast polarization is parallel to the margin within the asthenosphere. This suggests margin parallel flow beneath the plate. The lower oceanic lithosphere preserves paleo-spreading-parallel anisotropy, while the continental lithosphere has complex anisotropy reflecting several Wilson cycles. These results demonstrate the complex and active nature of a margin which is traditionally considered tectonically inactive.

Mantle structure and flow across the continent-ocean transition of the eastern North American margin: anisotropic *S*-wave tomography

Brennan R. Brunsvik[1*], Zachary C. Eilon[1], Colton Lynner[2]

[1]Department of Earth Science, University of California, Santa Barbara, CA, USA
[2]Department of Earth Science, University of Delaware, Newark, DE, USA

Key Points:

- We conducted mantle-scale velocity-anisotropy tomography across the continent-ocean transition of eastern North America.
- The results capture layers of anisotropy preserved from collision and extension, as well as produced from modern mantle flow.
- The imaged lithospheric and asthenospheric structure supports edge-driven convection and margin parallel asthenospheric flow.

*Department of Earth Science, Webb Hall, University of California, Santa Barbara, CA 93106

Corresponding author: Brennan Brunsvik, `brennanbrunsvik@ucsb.edu`

Abstract

Little has been seismically imaged through the lithosphere and mantle at rifted margins across the continent-ocean transition. A 2014-2015 community seismic experiment deployed broadband seismic instruments across the shoreline of the eastern North American rifted margin. Previous shear-wave splitting along the margin shows several perplexing patterns of anisotropy, and by proxy, mantle flow. Neither margin parallel offshore fast azimuths nor null splitting on the continental coast obviously accord with absolute plate motion, paleo-spreading, or rift-induced anisotropy. Splitting measurements, however, offer no depth constraints on anisotropy. Additionally, mantle structure has not yet been imaged in detail across the continent-ocean transition. We used teleseismic *S*, *SKS*, *SKKS*, and *PKS* splitting and differential travel times recorded on ocean-bottom seismometers, regional seismic networks, and EarthScope Transportable Array stations to conduct joint isotropic/anisotropic tomography across the margin. The velocity model reveals a transition from fast, thick, continental keel to low velocity, thinned lithosphere eastward. Imaged short wavelength velocity anomalies can be explained by edge-driven convection. We also find layered anisotropy. The anisotropic fast polarization is parallel to the margin within the asthenosphere. This suggests margin parallel flow beneath the plate. The lower oceanic lithosphere preserves paleo-spreading-parallel anisotropy, while the continental lithosphere has complex anisotropy reflecting several Wilson cycles. These results demonstrate the complex and active nature of a margin which is traditionally considered tectonically inactive.

Plain Language Summary

North America was once connected to Africa, but the continents rifted apart and are now separated by the Atlantic Ocean. The nature of rifting on land has been thoroughly studied. However, it is much more difficult to study the offshore region where the thinned continent pinches out and the tectonic plate transitions to sea-floor produced after continental breakup. Using a new dataset from ocean-bottom seismic stations, we construct a 3-D image of seismic wavespeeds, which are diagnostic of rock type and temperature. We also image seismic anisotropy, which is the directional dependence of seismic velocity. Anisotropy is often used as a proxy for the direction of stretching or mantle flow. We find wavespeed anomalies diagnostic of convective cells driven by a step in the thickness of the lithosphere. The anisotropy models suggests that, in this region, the mantle beneath the plates is currently flowing along the margin. Within the tectonic plates, the mantle preserves anisotropy developed during cycles of rifting and collision. These seismic wavespeed and anisotropy models demonstrate the complex and active nature of a continental margin that is traditionally considered tectonically inactive.

1 Introduction

Continental rifting (*e.g.,* McKenzie, 1978; Wernicke, 1985) and sea-floor spreading (*e.g.,* Hess, 1962; Vine & Mathews, 1963) are fundamental tectonic processes. The transition from continental rifting to the production of seafloor and thus continental drifting, however, remains unclear (*e.g.,* Kendall et al., 2005; Shillington et al., 2006; Van Avendonk et al., 2006; Crosby et al., 2008; Begg et al., 2009; Huismans & Beaumont, 2011; Yuan et al., 2017; Larsen et al., 2018). Seismic resolution across the rift-drift transition, particularly in the mantle, is extremely limited due to the sparsity of broadband ocean-bottom seismometers (OBSs) offshore at rifted margins.

The eastern North American passive margin (ENAM) is an excellent location to study the tectonics of the rifted continent-ocean transition (COT). ENAM is a mature passive margin resulting from the rifting of Pangaea at ~230-200 Ma (Withjack et al., 2012). There has been relatively little deformation at ENAM since the transition from rifting to continental drifting in the Jurassic (Schlische, 2003; Withjack & Schlische, 2005).

Structures associated with rifting along the margin are thus likely unperturbed and can offer insights into rifting processes.

ENAM is a natural laboratory for studying rifting processes (Worthington et al., 2021). It was selected as a primary site for a Geodynamic Processes at Rifting and Subducting Margins (GeoPRISMS) community seismic experiment (CSE) (Lynner et al., 2020). Thirty broadband OBSs were deployed in 2014-15, while the Transportable Array (TA) was in the eastern US (Figure 1). The TA provided excellent on-land broadband seismic coverage in the eastern US throughout 2012-2015, supporting interrogation of the continent. Combined, the ENAM-CSE and TA provide dense, co-temporal seismic data coverage crossing the COT. The ENAM-CSE constitutes one of the only rifted-margin crossing broadband OBS datasets, which is capable of interrogating a rifted COT in the mantle. This dataset has already been utilized for crustal-scale ambient noise tomography (Lynner & Porritt, 2017; Li & Gao, 2019), shear-wave splitting analyses (Lynner & Bodmer, 2017), multi-channel reflection imaging (Bécel et al., 2020), and crustal to uppermost-mantle tomography based on wide-angle seismic data (Shuck et al., 2019). However, no margin-spanning body-wave velocity or 3-D anisotropy models have been developed that illuminate the offshore mantle with the coverage offered by these OBSs, leaving mantle structure and flow across the COT largely unknown.

1.1 The ENAM continent-ocean transition

During continental breakup, the lithosphere thins (*e.g.,* Wernicke, 1985; Ziegler & Cloetingh, 2004; Crosby et al., 2008; Huismans & Beaumont, 2011). However, it is unknown whether there is a transition in plate thickness, wavespeed, or other properties across the ENAM COT. It is also unknown to what extent the oceanic lithosphere has thermally grown in with time. It is not known whether the lithosphere-asthenosphere boundary bears a signature of the COT (*e.g.,* Yuan et al., 2017) because the lithospheric and mantle structure at the COT has not been imaged in detail.

Several studies have used dense on-land seismic coverage to image the ENAM continental crust and mantle (*e.g.,* Forte et al., 2007; Van Der Lee et al., 2008; Bedle & van der Lee, 2009; Schmandt & Lin, 2014; Biryol et al., 2016; Pollitz & Mooney, 2016; Savage et al., 2017; Golos et al., 2018; Wagner et al., 2018; Savage, 2021). These informed the continent's lithospheric structure, which contains a mid-lithospheric discontinuity in the continental interior, thins toward the ocean, and is highly thinned at the Harrisonburg anomaly (HA) in Virginia (*e.g.,* Abt et al., 2010; Byrnes et al., 2019; Savage, 2021). However, studies to date have focused primarily on continental structures and have not incorporated the new OBS data.

Utilizing ENAM-CSE OBSs, recent Rayleigh wave ambient noise phase velocity tomography has shown crustal thinning across the margin and a correlation between the East Coast Magnetic Anomaly (ECMA) and a region of thinned crust (Lynner & Porritt, 2017). Full-waveform ambient-noise tomography reinforced these results (Li & Gao, 2019). The presence of the ECMA at the edge of the margin suggests that it is correlated with the first oceanic material emplaced after rifting. Active source results show that the crust is thin (down to about 6-8 km) and highly faulted between the ECMA and the Blake Spur magnetic anomaly (BSMA) (Shuck et al., 2019; Bécel et al., 2020), which is approximately 100-200 km east of the ECMA. The localized, thin crust suggests that a ~ 150 km swath of crust between the magnetic anomalies is proto-oceanic and formed during ultra-slow spreading. The crust thickens to about 8.5-10 km and attains a smoother topography at the BSMA. This may imply that full sea-floor spreading did not initiate until the emplacement of BSMA (~ 170 Ma).

Ambient noise surface waves and long-offset refraction data are primarily sensitive to structure in the crust. The relationship of the lithospheric mantle wavespeed structure and crystalline fabric to crustal structure, magnetic anomalies, and stages of rift-

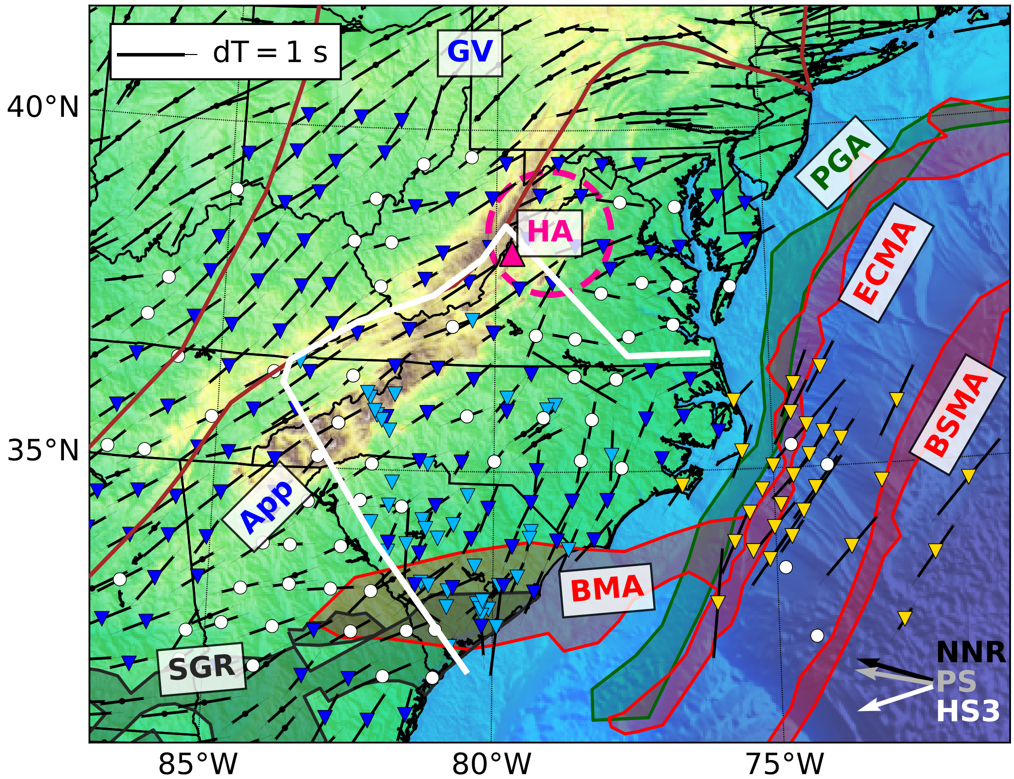

Figure 1. Map of the study area, showing stations used in our inversion (inverted triangles and white circles) and previous splitting measurements (Long et al., 2016; Lynner & Bodmer, 2017; Yang et al., 2017) that we averaged at each station. Splitting measurements are black lines centered at stations. Stations with dominantly null splitting are white circles. These null splitting stations had quality null arrivals and no split arrivals in Lynner and Bodmer (2017) and Long et al. (2016), but may still have split arrivals in Yang et al. (2017). For non-null splitting stations, the OBSs and land stations that were deployed as part of the ENAM-CSE are yellow triangles, the TA is dark blue triangles, and other networks are light blue triangles. The white line shows the boundary between stations where we measured splitting and stations where we only measured differential travel times. We also show splitting averages outside our seismometer array, where stations are indicated as small black dots. The Appalachian (App) and Grenville (GV) province boundaries are indicated by brown lines. The low velocity Harrisonburg anomaly (HA) is indicated with a pink, dashed circle (HA location is from our results; see also Biryol et al., 2016; Pollitz & Mooney, 2016; Savage, 2021). The pink triangle is the approximate location of Eocene volcanics (Mazza et al., 2014). Arrows at bottom right show approximate directions of Paleo-spreading (PS) (Becker et al., 2014) and plate-motion in no-net-rotation (NNR; DeMets et al., 2010) and hot-spot (HS3; Gripp & Gordon, 2002) reference frames. We highlighted the Positive Gravity anomaly (PGA) based on Sandwell and Smith (2009). We highlighted magnetic anomalies (BMA, ECMA, BSMA) based on Maus et al. (2009). South Georgia Rift basin (SGR) modified from Akintunde et al. (2014) and Chowns and Williams (1983). OBSs: ocean-bottom seismometers. ENAM-CSE: Eastern North American margin community seismic experiment. TA: Transportable Array. HA: Harrisonburg anomaly. SGR: South Georgia Rift basin. App: Appalachian. GV: Grenville province. BMA: Brunswick Magnetic Anomaly. PGA: Positive Gravity Anomaly. ECMA: East Coast Magnetic Anomaly. BSMA: Blake Spur Magnetic Anomaly. PS: Paleo-spreading direction. NNR: No-net-rotation reference frame. HS3: Hot-spot reference frame.

ing remains unknown. Here, we image the structure of the lithosphere at the COT. We investigate how the structures are associated with the transition from continental break up to continental spreading and how the lithosphere has subsequently been modified.

1.2 Mantle flow

Several important geodynamic phenomena have been proposed at ENAM (*e.g.,* Long et al., 2010). Fouch et al. (2000) showed that shear-wave splitting within the continent is consistent with a model where mantle flow is redirected by a deep continental lithospheric keel to flow perpendicular to the margin. Low shear velocity near ENAM could indicate volatile abundance and upwelling material associated with subducted Farallon slab (Van Der Lee et al., 2008). The strong horizontal temperature gradient in the mantle near the cratonic edge (the "keel") can induce edge-driven convection (EDC) (*e.g.,* King & Ritsema, 2000; Ramsay & Pysklywec, 2011; Savage et al., 2017). EDC has been invoked to explain specific seismic velocity features at ENAM (*e.g.,* Savage et al., 2017). Conversely, the slow velocity features may indicate lithoshperic delamination and asthenospheric upwelling, which could also account for enigmatic Eocene volcanism (Figure 1; *e.g.* Mazza et al., 2014; Biryol et al., 2016). Margin-parallel shear-wave splitting results offshore have been interpreted as reflecting large scale density-driven flow (Lynner & Bodmer, 2017).

Observational constraints on mantle flow at ENAM, particularly beneath the ocean, are limited (*e.g.,* Yuan et al., 2011; Lynner & Bodmer, 2017; Yang et al., 2017). Seismic anisotropy is a crucial observational constraint on mantle flow. Our joint velocity/anisotropy tomography model, with sensitivity extending through the asthenosphere, is poised to address mantle flow near the COT of ENAM.

1.3 Anisotropy and shear-wave splitting

Seismic anisotropy measurements can offer insight into patterns of mantle deformation (*e.g.,* Silver, 1996; Long & Becker, 2010; Skemer & Hansen, 2016). Deformation via dislocation creep produces a crystallographic preferred orientation (CPO) due to heterogeneity in the strength of internal slip systems (Karato & Wu, 1993; Maupin & Park, 2007; Karato et al., 2008). Olivine CPO produced in this way is one of the dominant anisotropic signatures associated with mantle flow. Other phenomena can also result in seismic anisotropy, including aligned fractures or melt pockets (*e.g.,* Vauchez et al., 2000; Kendall et al., 2005).

Shear-wave splitting is a common method used to examine seismic anisotropy (Silver & Chan, 1991). Solutions to the Christoffel equation generally give three wave speeds and particle motion polarizations corresponding to a P wave and two quasi-S waves (Maupin & Park, 2007). Because the quasi-S waves travel at different velocities in an anisotropic medium, a time delay between them can accrue. Using the polarization and time delay between the quasi-S waves, the strength and orientation of anisotropy can be inferred.

There is a first-order question across the ENAM whether CPO fabrics and anisotropy are dominated by recent processes or record deformation associated with continental breakup. If associated with recent processes, splitting may align with absolute plate motion or paleo-spreading in the ocean (*e.g.,* Silver, 1996; Long et al., 2010; Becker et al., 2014). If related to past deformational events, splitting may align with tectonic boundaries (*e.g.,* Silver, 1996; Long et al., 2010). *SK(K)S* phase splitting across the ENAM exhibits a complex pattern of anisotropy that does not fit with either simple explanation. A region of dominantly null and very weak splitting on the continent (Figure 1; Wagner et al., 2012; Long et al., 2016) might be caused by roughly isotropic material, vertical mantle flow, or depth varying anisotropy that effectively cancels. Further, splitting at the OBSs reveals margin-parallel fast-axes (Figure 1; Lynner & Bodmer, 2017). This is neither consistent with paleo-spreading parallel frozen-in anisotropy in the lithosphere nor absolute-plate-motion-parallel anisotropy in the sheared asthenosphere (*e.g.* Becker et al., 2014). Lynner and Bodmer (2017) proposed the splitting is a consequence of modern margin parallel mantle flow. However, splitting of *S(K)KS* phases provides few constraints on the depth of anisotropy in the upper mantle, making it difficult to interpret what geodynamic processes are occurring (*e.g.,* Long et al., 2016; Lynner & Bodmer, 2017; Yang et al., 2017).

In this paper, we provide the first high resolution constraints on 3-D anisotropy and velocity heterogeneity across the COT of the rifted ENAM with sensitivity through the lithosphere-asthenosphere system. We obtained improved anisotropic depth resolution by combining *S*-phase splitting (*e.g.,* Hammond & Toomey, 2003; Boyd et al., 2004) with *S(K)KS* and *PKS* phases in a tomographic method (Eilon et al., 2016). We used a 1500-km-wide seismic array of broadband stations to produce a model that extends from the Appalachians to $\sim$ 300 km offshore (Figure 1). We interrogate anisotropy that developed during previous tectonic events, and utilize anisotropy to inform modern asthenospheric flow. We utilize isotropic velocity heterogeneity to interrogate the structure of the mantle, which further informs geodynamic processes, as well as to understand the lithospheric-scale structure of the rift and transition from continent to ocean.

2 Methods

We applied a joint velocity and anisotropy tomography method which uses differential travel times and splitting times of *S*, *SK(K)S*, and *PKS* phases to simultaneously solve for 3-D seismic velocity (synonymous with wavespeed) and azimuthal anisotropy (Eilon et al., 2016). Inversions which assume no anisotropy can produce significantly biased velocity models (Bezada et al., 2016). In addition to providing new depth constraints on anisotropic structure, an important strength of this approach is that it addresses the trade-off between anisotropic and isotropic controls on travel times (Eilon et al., 2016).

We used broadband data from the ENAM-CSE (up to 1.5 years of data from 30 OBSs and 3 land seismometers), the Transportable Array (TA) (which was present in the eastern U.S. from 2011-2015), and several regional networks for a total of 245 stations (Figure 1). Our earthquake selection criteria (Section S1.1) leave 2326 earthquakes which we evaluated from January 2003 to May 2020.

We first measured shear wave splitting times jointly with differential travel times (Section 2.1). We used an augmented multi-channel cross-correlation (MCCC) approach (Eilon et al., 2016). Splitting times were measured as either margin-parallel fast (positive) or margin-perpendicular fast (negative) (Figure 2). Splitting times constrain anisotropy. We jointly measured differential travel times, relative to the arrival times predicted by the IASP91 1-D velocity model (Kennett & Engdahl, 1991), between all stations. The primary role of the differential travel times is to constrain isotropic velocity, although they also inform anisotropy.

Splitting and differential travel times were the input for the tomographic method (Section 2.2; Figure 3, 4, and 5). We decompose velocities into margin parallel ($V_\parallel$) and perpendicular ($V_\perp$) components (Figure 4). We jointly invert these velocities using our splitting and differential travel times (Eilon et al., 2016). Isotropic velocity is simply $\left(V_\parallel + V_\perp\right)/2$. Velocity is reported as percent deviation from each layer's average. Differential travel times cannot constrain absolute velocity; by construction, velocity deviations within each layer have an average of zero. Azimuthal anisotropy strength is simply $\left(V_\parallel - V_\perp\right)/\left(V_\parallel + V_\perp\right)$, so positive values indicate margin-parallel fast and negative values indicate margin-perpendicular fast (Figure 4).

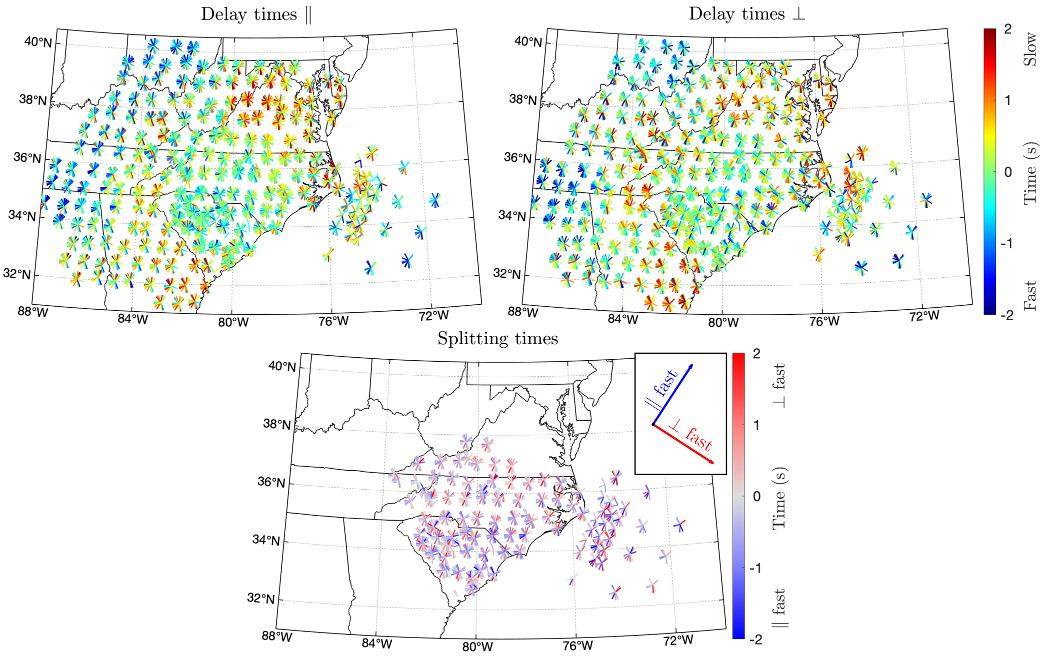

Figure 2. Inverted differential travel times for teleseismic *S*, *S(K)KS*, and *PKS* phases polarized parallel and perpendicular to the symmetry axis, $\delta T_{\parallel}$ and $\delta T_{\perp}$, as well as the measured splitting times, dT_{splt}. Each measurement is plotted as a line that points toward the earthquake. Note that smaller array bounds are used for measuring splitting to avoid anisotropy with non-constant geometries.

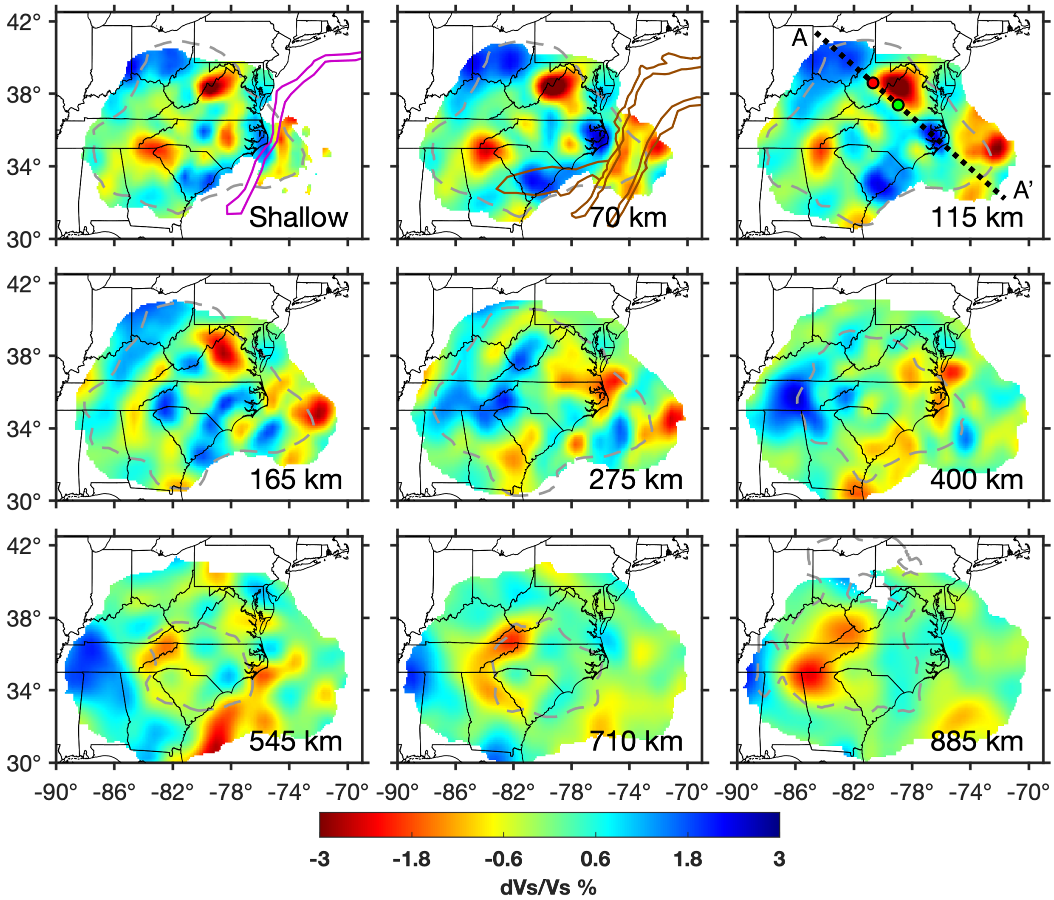

Figure 3. Final isotropic shear velocity model. Each layer shows percent deviation from the layer's average velocity. "Shallow" is our shallowest layer. It contains structure which is too shallow to be vertically resolved and is essentially averaged above ∼ 70 km. Positive Gravity Anomaly (PGA), drawn based on Sandwell and Smith (2009), shown on shallow depth slice as magenta line. Magnetic anomalies, drawn based on Maus et al. (2009), shown on 70 km slice as brown lines. From west to east, they are the BMA, ECMA, and BSMA. Models are only plotted where hit quality exceeds 0.7. The dashed gray contour shows where semblance (a measurement of the similarity between synthetic input and output checkerboard models) exceeds 0.8. Red and green dots on the 115 km slice border the high topography region of the Appalachians. PGA: Positive Gravity Anomaly. BMA: Brunswick Magnetic Anomaly. ECMA: East Coast Magnetic Anomaly. BSMA: Blake Spur Magnetic Anomaly.

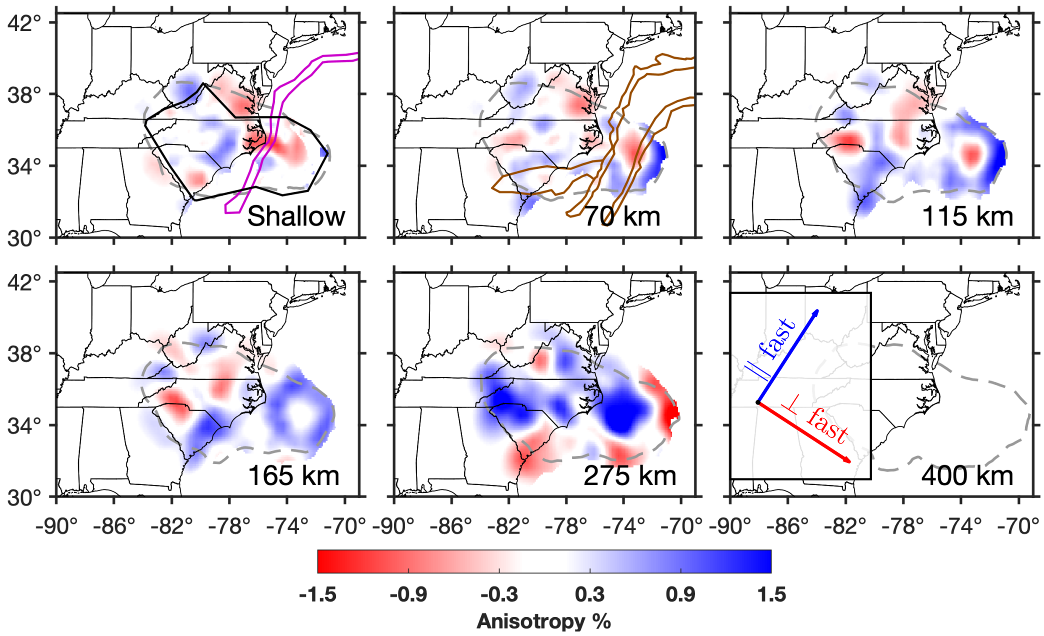

Figure 4. Final anisotropy model. See Figure 3 for description of shallow layer, potential field contours, and masking based on hit quality and semblance. Blue indicates margin-parallel-fast anisotropy and red indicates margin-perpendicular-fast anisotropy. Anisotropy is assumed to be 0 beneath 300 km. The black contour on the "shallow" slice is the region within which we measured splitting times.

2.1 Anisotropic multi-channel cross-correlation

To jointly measure splitting and differential travel times, we used the augmented multi-channel cross-correlation (MCCC) method of Eilon et al. (2016). This augmented method builds on traditional MCCC (Section S1; VanDecar & Crosson, 1990). We assume a constant horizontal hexagonal symmetry axis with orientation $\phi =$ N33°E. The fixed symmetry axis is not equivalent to assuming a fixed fast splitting orientation. Rather, we assume that structure will be organized according to the tectonic geometry: either margin-parallel or margin-perpendicular fast. This geometry is seen in the OBS splitting measurements (which have an average fast polarization of N33°E: Lynner & Bodmer, 2017) as well as splitting measurements in the Appalachians (Figure 1; Long et al., 2016). The assumed anisotropy can produce split quasi-S waves polarized approximately parallel and perpendicular to ϕ. These have differential travel times $\delta T_{\parallel}$ and $\delta T_{\perp}$, respectively. The difference between these times at a station is the splitting time dT_{splt}. By incorporating both quasi-S waves into MCCC, we simultaneously measured all three delay times. In detail, the relative amplitude of both quasi-S waves, and thus the feasibility of measuring splitting, depends on a wave's particle motion polarization (Section S1.2). For some earthquakes, we can only measure $\delta T_{\parallel}$ or $\delta T_{\perp}$.

We require a constant assumed symmetry axis direction for the tomography method to work. We evaluated whether the preponderance of SKS splits at any station is concordant with the assumed symmetry. This is quantified as previous splitting fast polarizations being on average within $\sim 25°$ of parallel or perpendicular to the assumed symmetry axis (Figure S1). We only measured splitting times and carry out anisotropic tomography in this region. Outside this region, we measured differential travel times only and conducted only isotropic tomography, fixing anisotropy to zero (Figure 2 and 4). Fi-

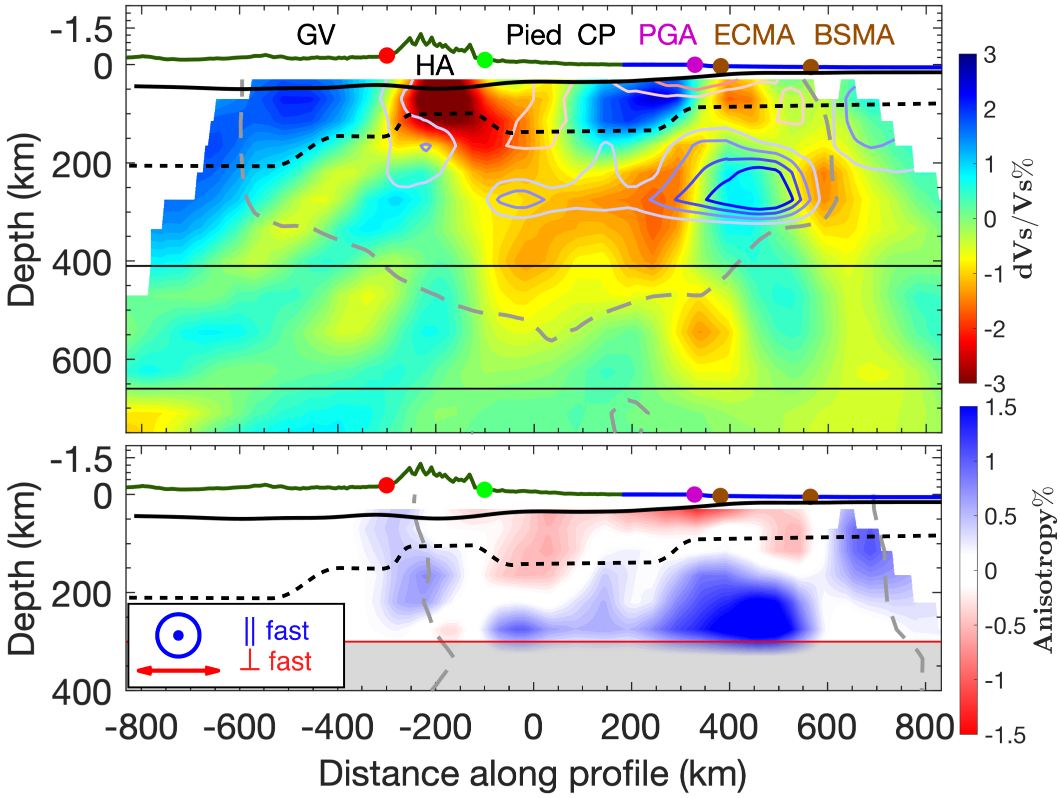

Figure 5. Cross-sections of the velocity (top) and anisotropy (bottom) models. Contours of anisotropy are shown on top of the velocity figure at $\pm 0.4\%, 0.75\%, 1.1\%$, and 1.45%. Elevation lines are blue in the ocean and green on land. The red and green dots on the elevation line correspond to the same dots in Figure 3. Mantle transition zone lines are shown at 410 km and 660 km. The approximate dislocation creep regime base is indicated as a red line at 300 km depth. We assumed no anisotropy beneath 300 km, which is greyed out. The Moho depth (Shen & Ritzwoller, 2016; Shuck et al., 2019) is shown as a solid black line. The approximate, interpreted lithosphere-asthenosphere boundary is shown as a black dashed line. Cross-sections run from northwest to southeast (A-A' in Figure 3). Only portions of the model where the hit quality is greater than 0.7 is shown. The dashed gray contour shows where semblance (a measurement of the similarity between synthetic input and output checkerboard models) exceeds 0.8. GV: Grenville province. HA: Harrisonburg anomaly. Pied: Piedmont. CP: Coastal plains. PGA: Positive Gravity Anomaly. ECMA: East Coast Magnetic Anomaly. BSMA: Blake Spur Magnetic Anomaly.

nally, we down-weighted splitting measurements made where the measured symmetry axis deviates from our assumed symmetry axis. We weighted measurements by $\sqrt{|(45° - \Delta\phi)|/45°}$ where $\Delta\phi$ is the difference between our assumed symmetry axis and the mean fast polarization of literature measurements within the proximity of a station ("splitting misorientation" in Figure S1).

Our method also assumes that symmetry axes are horizontal, and it is not sensitive to radial anisotropy. Any radial anisotropy will be mapped into our results, but only weakly. This effect is well within the uncertainty of the data (Eilon et al., 2016). Variations in anisotropy orientation with depth could be further problematic. A lack of strong back-azimuthal variability in splitting measurements offers some support that layered anisotropic fabrics are either parallel or perpendicular to each other where we measure splitting times (Yang et al., 2017). Our method is optimal for such layering. We verified that the complexity of splitting at ENAM is consistent with our simplified anisotropic orientation, supporting that the first order azimuthal anisotropy can be captured by our inversion.

The supplementary information (Section S1) describes quality control and data processing steps used when measuring splitting and travel times, as well as how we incorporated multiple MCCC datasets for different sub-regions (Section S1.1), along with splitting measurements from the literature (Long et al., 2016; Lynner & Bodmer, 2017; Yang et al., 2017).

2.2 Tomography

We jointly inverted the velocity and anisotropy models using the splitting and differential travel times. It is not feasible to independently resolve the number of parameters required to describe even relatively simple hexagonal anisotropic elasticity. This is largely due to inherent non-linearities and the limits of the data. Instead, we followed the methodology of Eilon et al. (2016) in applying several key assumptions to parsimoniously parameterize the anisotropic elastic tensor (Section S2). This approach reduces the required parameters at each model node to two: the velocities of shear waves traveling vertically with particle motion polarities parallel ($V_{\|}$) and perpendicular ($V_{\perp}$) to the anisotropic symmetry axis. These parameters easily translate to isotropic velocity and anisotropy. Based on simplified formulae for Vsh and Vsv (Section S2), we then calculated the differential travel times ($\delta T_{\|}$, $\delta T_{\perp}$), and splitting times (dT_{splt}).

We applied *a priori* crustal corrections to account for the influence of known crustal heterogeneity on differential travel times (Section S3; Figure S2; *e.g.,* Sandoval et al., 2004). We additionally solved for event and station static terms for splitting and differential travel times (Section S3). The static terms account for heterogeneity outside the model. We accounted for finite frequency effects using a first Fresnel zone paraxial approximation (Section S4), which is updated from Schmandt and Humphreys (2010) and Eilon et al. (2015).

The discretization and ray geometry influence where the model is reliably recovered. The model space extends from 30 km to 1080 km depth, with inter-node vertical spacing that increases linearly with depth from 40 km to 100 km. Above the depth where rays cross (~ 70 km), the inversion cannot accurately constrain the depth of heterogeneity. The delay times are still sensitive to structure in this depth range, and structure here will be mapped into station static terms or the shallow portion of the model. We display the 30 km "shallow structure" layer (Figure 3 and 4) because, although structure here is formally not vertically resolved, this layer still illuminates important lateral heterogeneity. The horizontal span of the model is between latitudes 25°N and 46°N and longitudes 96°W and 63°W. This includes a buffer region beyond the seismic array on all sides, required for well-behaved tomography. We do not interpret or display structure in this buffer region. Horizontal node spacing within the seismometer array is 40 km.

We addressed the mixed-determined tomographic inverse problem using smoothed, damped, least squares (*e.g.,* Menke, 2012). This is equivalent to imposing *a priori* assumptions of relatively simple structure and relatively modest perturbations in velocity and anisotropy. We used "L-tests" to determine the appropriate regularization parameters (Section S5; Figure S3).

Anisotropy in the upper mantle is dominantly controlled by the CPO of olivine. This conventionally develops through deformation within the dislocation creep regime. However, with increasing depth, the dominant deformation mechanism of olivine in the mantle transitions from dislocation to diffusion creep (Karato & Wu, 1993). In 1-D Earth reference models, anisotropy (Vsh/Vsv) tends toward zero by about 300 km depth (Chang et al., 2015). This is much shallower than the base of our model. To prevent erroneous mapping of anisotropy to depths where CPO, and hence anisotropic fabrics, is unlikely, our preferred models assume zero anisotropy beneath 300 km depth. For completeness, we also present models where this assumption is relaxed (Figure S4 and S5). As expected, in this case, anisotropy extends deeper than the anticipated dislocation creep regime. However, we find that upper mantle features that we interpret remain.

We evaluated how simplifications regarding wave polarization in the forward model (Section S2) might bias the data fit. We conducted a synthetic splitting test with a more complete parameterization. We propagated Gaussian pulses through our anisotropic model along a given ray path, solving the full Christoffel equation in each layer to find quasi-S wave velocities and polarizations. These calculations utilized the back-azimuths and ray parameters from the actual data. In each layer, we sequentially apply splitting to the wavelet. At the top of the model, we measured splitting parameters on the final synthetic waveform using transverse energy minimization, mimicking the processing of real splitting data (Silver & Chan, 1991). Figure S6 shows one example resulting transverse energy surface. The resulting synthetic fast polarizations closely match observed splitting fast polarizations from the literature over the vast majority of the region (Figure 6). The only notable exception is in the north of our model, where isolated synthetic split fast polarizations approach orthogonal to their literature counterparts. This mismatch is primarily at stations where Long et al. (2016) measured only nulls. Other Splitting measurements in the literature become highly variable here, for example rotating from margin parallel to perpendicular across the MAGIC array just north of our study region (Aragon et al., 2017). Our synthetic splitting delay times are small here ($<\sim 0.3$ s), which is consistent with previous null measurements at those stations, and we place low emphasis on the polarization of the almost null synthetic splits.

3 Results

3.1 Delay times and shear wave splitting

We used MCCC to measure splitting and differential travel times. The well-aligned and linearized waveforms after undoing the effects of splitting indicate success of the approach (Figure S7). Weighted variance reduction for differential travel times ($\delta T_{\parallel}$ and $\delta T_{\perp}$) is 66.4%, and for splitting times (dT_{splt}) is 74.3%. On average, particle motion ellipticity for splitting-corrected shear waves is 51% the original ellipticity. We calculated ellipticity as the ratio of eigenvalues in the particle motion covariance matrix (*e.g.,* Silver & Chan, 1991). Of the 2326 earthquakes, we applied MCCC to 742, yielding $48,428$ delay and splitting measurements (Figures 2 and S8). The remaining earthquakes were rejected based on the quality control criteria (*e.g.*, poor signal-to-noise ratio or poorly aligned waveforms after applying MCCC: Section S1.1).

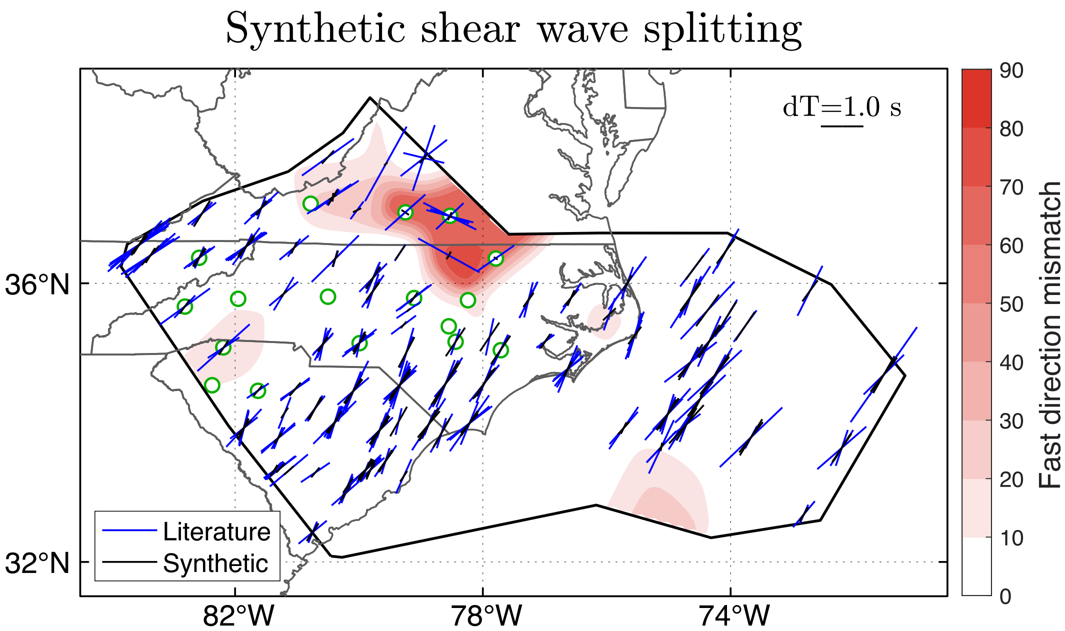

Figure 6. Results of synthetic splitting tests applied to rays for which splitting has been measured in the literature (Long et al., 2016; Lynner & Bodmer, 2017; Yang et al., 2017). We calculated these by first synthetically splitting waveforms and then measuring splitting using transverse energy minimization. This synthetic splitting method is not dependent on the simplifying assumptions regarding waveform polarization from Section 2.2 and S2. The orientations of black and blue lines indicate fast polarizations, and line lengths indicate splitting delay times. Background color indicates the angular misorientation between our synthetic splits and splitting measurements from the literature, which is interpolated to 2-D using a Gaussian filter. Green/white circles indicate stations identified as null splitting stations in Long et al. (2016). We did not apply this analysis where we did not measure splitting, outside the thick black line.

The differential travel times show up to ~ 1.5 s fast arrivals in the Grenville orogenic belt and up to ~ 1.3 s slow arrivals at the Harrisonburg Anomaly (HA) near the Virginia/West Virginia border (Figure 2 and S8). The splitting times indicate dominantly margin-parallel-fast splitting offshore. They also show dominantly margin-parallel-fast anisotropy near North/South Carolina within a region encompassed by small splitting times, consistent with Long et al. (2016). Different from most previous literature, we measured margin-perpendicular splitting over parts of the coastal plains (*e.g.,* Long et al., 2016; Yang et al., 2017). However, these measurements are consistent with the transition from margin parallel to perpendicular splitting moving oceanward across the MAGIC seismometer array north of our study region (Aragon et al., 2017). Splitting measurements can often be resolved only if the delay times are fairly large (*e.g.*, at least 0.5 s splitting using periods longer than 8 s in Long et al., 2016). MCCC improves precision over single station measurements (VanDecar & Crosson, 1990), allowing us to identify splitting trends where splitting times are small.

3.2 Resolution

We conducted synthetic checkerboard resolution tests with approximately 2° sized checkers (Figures S9 and S10). Beneath 300 km, structure is more smeared and reduced in amplitude, but is still recovered. The edges of the plotted model are notably less well resolved than the center by ~ 400 km depth. While velocity heterogeneity is partially resolved beneath 400 km onshore, Figure S9 suggests we should not interpret > 400 km deep velocity anomalies offshore. Anisotropy checkers are well resolved above 300 km.

We calculated semblance, comparing the original and inverted checkerboard models within 260 km radius from each model node (Zelt, 1998). We found semblance > 0.8 corresponds to checkers that we consider well resolved (Figure S9 and S10). We do not interpret, and suggest caution, regarding features where semblance is lower. Hit quality assesses the number of and back-azimuthal distribution of rays throughout model. We do not plot the model where hit quality < 0.7 (this value is roughly consistent with semblance < 0.8 in the shallow part of the model).

We conducted spike tests to further assess resolution (Section S6; *e.g.,* Rickers et al., 2013; Rawlinson & Spakman, 2016). These approximate the impulse response of the inversion (Menke, 2012). We used a spherical spike centered at 165 km depth with 85 km radius (Figure S11 and S12). The output structures had vertical smearing over approximately 200 km (Figure S11 and S12). Velocity and anisotropy amplitude was reduced by $\sim 40\%$. Smearing and reduced amplitude are normal consequences of damping and smoothing. The spike test demonstrates independence of anisotropy and velocity. For the velocity spike test with 0% anisotropy input, the maximum inverted anisotropy magnitude was 0.15%. The anisotropy spike test showed maximum inverted dV of 0.06%. The basic input structure is clearly represented in the output structures, despite some normal distortions.

Squeezing tests indicate the depth to which the data require structure (Section S7; Figure S13). They suggest that velocity heterogeneity is required to at least 660 km depth, which is the limit of our interpretations. Squeezing tests also suggests that noise and velocity-anisotropy trade-off are erroneously mapped toward to base of the anisotropy model. This corroborates our decision to enforce zero anisotropy beneath 300 km depth, the approximate dislocation creep regime depth (Chang et al., 2015).

3.2.1 Synthetic resolution tests for specific features

To understand how specific features of interest might be imaged in our models, we conducted synthetic input-output tests using structures which match different regional predictions (Figure S14 and S15). We included features within our final models which we seek to interpret. Key input velocity features included a fast, thick, Precambrian lithosphere in the northwest of the model and the slow Harrisonburg Anomaly (HA) (Figure S14). The main features we interpret, above about 400 km, are all well resolved. The HA was recovered with smearing over approximately 100 km. High velocity anomalies at the continent-ocean transition (COT) were recovered well. Two deep anomalies within our models, a high velocity anomaly centered near 500 km depth and a low velocity anomaly centered near 800 km, were recovered in shape but with only about 30% of their original amplitude. This suggests caution for interpreting mantle transition zone and deeper mantle features, which are not our focus.

The anisotropy input models included two scenarios (Figure S15). For the offshore region, we tested 1.5% paleo-spreading parallel (margin-perpendicular) fast frozen-in lithospheric anisotropy overlying an equal magnitude margin parallel mantle-flow induced anisotropy. In the continent, we tested a lithospheric layer overlying an asthenospheric layer. This anisotropy could cause previously observed null splitting (Long et al., 2016). Both layers were recovered offshore with approximately 50% amplitude loss and a lateral limit to good lithospheric layer recovery about 200 km from the continent. The continental layers were recovered with similar amplitude loss but with better shape preservation. These tests are strong evidence that first order anisotropic mantle structure, including depth variations, should be faithfully imaged by our models.

3.3 Tomography results: isotropic velocity models

The shear velocity models can be seen in Figure 3, 5, S16, and 3-D models can be viewed interactively using the supplementary linked file `brunsvik-tomog.html`. A prominent fast velocity structure is observed furthest into the continent above about $200-300$ km depth (extending to a maximum depth of ~ 400 km). This structure is as much as 2% fast compared to any layer's average. Within the +1% velocity isosurface of this feature, the mean wavespeed is +1.5%. The shallower ($<\sim$200 km depth) portion of this is the cold, thick, continental interior lithosphere (*cf.* Savage, 2021). However, this feature is near the edge of our array and only its basic structure is clear (Figure S9). The high velocity lithosphere shallows toward the ocean until it meets the most prominent slow-velocity feature in our model, in Virginia ($\sim 38.5°$N, 79°W). This is the previously imaged low-velocity Harrisonburg anomaly (HA) (*e.g.,* Shen & Ritzwoller, 2016; Savage et al., 2017; Wagner et al., 2018). This feature dips oceanward from the surface. It is up to $\sim 5\%$ slow at 70 km depth. The average velocity within the -1% slow isosurface of the HA is -1.9%. Oceanward of the HA, from ~ -100 to 350 km horizontally in Figure 5, we observe a low velocity anomaly just above the 410 km transition zone. This feature appears to connect to the HA.

Several features in the model correspond with magnetic and gravity anomalies. A high velocity feature (up to $\sim 2\%$ fast at 70 km depth) in southern Georgia closely follows the trend of the Brunswick Magnetic Anomaly (BMA) and South Georgia Rift (SGR) (Figure 1 and 3). Beneath the OBSs, upper mantle velocity tends to be slower than on the continent. The offshore 70 km layer is 0-2% slow compared to the whole layer average. A low velocity band above ~ 100 km closely follows the trend of the East Coast Magnetic Anomaly (ECMA) and Positive Gravity Anomaly (PGA). This is in the better resolved portion of the offshore region, though resolution of such a fine structure is suspect given our recovery tests (Figure S9). We also note a low velocity feature, near the edge of the array and thus likely poorly resolved, that correlates with the Blake Spur Magnetic Anomaly (BSMA) (Figure 3). With caution regarding reduced ray coverage offshore, increased delay/splitting noise, and synthetic test results (Figure S9), we focus our interpretation on only the dominant trends offshore. Some oceanic structures may be artifacts at the edge of our seismometer array. For instance, the nearly 3% slow anomaly at 72°W, 35°N, and 165 km depth is likely an artifact (Figure 3 and S16).

We also observe anomalies deep in the mantle. Checkerboard tests (Figure S9) suggest not to interpret the low velocity anomalies at 545 km depth offshore of Georgia and Florida. These features are outside the semblance > 0.8 contour (Figure 3 and S9). The $< 3\%$ fast velocity anomaly that is strongest beneath Tennessee near ~ 400 km depth has been previously imaged (*e.g.,* Schmandt & Lin, 2014; Biryol et al., 2016). We do not interpret the strong anomalies beneath about 660 km, which are less well resolved (Figure S9) and may be a result of using steeply incident *SK(K)S-PKS* rays. Nevertheless, other body wave tomography models similarly show strong anomalies at such depths here (*e.g.,* Schmandt & Lin, 2014; Golos et al., 2018; Wang et al., 2019).

3.4 Tomography results: anisotropy models

The anisotropy models can be seen in Figure 4, 5, S16, and interactively in the supplemental linked file `brunsvik-tomog.html`. As a key result, we observe two layers of anisotropy, both onshore and offshore (Figure 5). Deeper than $\sim 100-150$ km offshore, approximately within the asthenosphere, anisotropy is dominantly margin parallel (generally $> 1\%$ fast). In the offshore lower lithosphere, anisotropy is generally margin-perpendicular/paleo-spreading parallel, up to about 0.8% fast. Our results do not place depth constraint on upper lithospheric anisotropy, and are instead primarily sensitive to the lower lithosphere. The cross-section in Figure 5 runs through the center of the OBSs to give the most reliable sense of offshore anisotropy. However, lithospheric/asthenospheric layering becomes increasingly inconsistent away from the cross-section, where hit quality and resolution decrease (Figure 4). We suggest the model is strong evidence for lithosphere-asthenosphere anisotropic layering.

On the continent, our model shows margin-parallel-fast anisotropy in the asthenosphere ($> 1\%$ fast at 275 km depth) (Figure 4 and 5). This is consistent with dominantly margin parallel splitting from previous work (*e.g.,* Yang et al., 2017). At 165 km depth and above, the model shows some margin-perpendicular anisotropy up to almost 1% fast in the Piedmont and coastal plain (North/South Carolina and Virginia). This is the same region where Long et al. (2016) observed dominantly null splitting. This shallower anisotropy is complex, pocketed with ~ 100 km wavelength features. Margin-perpendicular-fast anisotropy is consistent with the *Pn* analysis of Buehler and Shearer (2017), which indicates margin-perpendicular-fast anisotropy just beneath the Moho in the coastal plain. This is also consistent with anisotropic surface-wave phase velocities in the low topography region east of the Appalachians, which rotate from margin parallel for periods longer than about 77 s to margin perpendicular for periods between about 77 s and 40 s (Wagner et al., 2018). The continental lithosphere has complicated anisotropy, while asthenospheric anisotropy is dominantly margin parallel.

4 Discussion

Our shear velocity and anisotropy models inform hypotheses of rift and drift dynamics, as well as interpretations of present day structures and processes. We first discuss the velocity and anisotropy structures associated with rifting. Second, we discuss the transition from rifting to drifting. Third, we discuss processes and structures which likely occurred and developed during and after the formation of the passive margin. Finally, we discuss the complex relationship between strain and anisotropy. Our observations and interpretations are summarized in Figure 7.

4.1 Rift structure

Our velocity models show thick Precambrian lithosphere in the northwest, which thins toward the margin (Figure 3 and 5). At the HA, the lithosphere is greatly thinned. However, the precise depth of the lithosphere-asthenosphere boundary is not easily es-

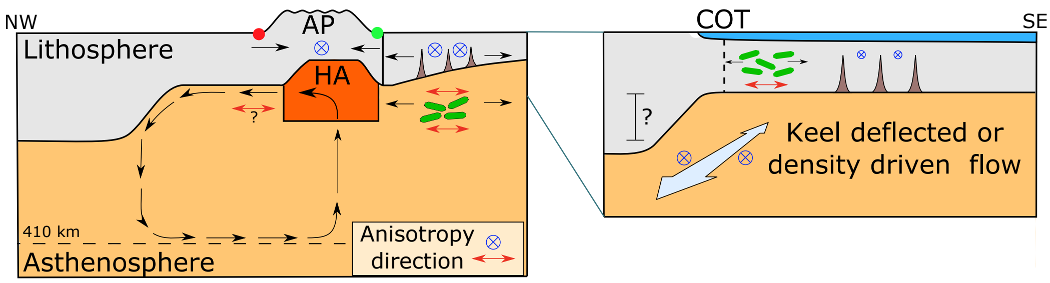

Figure 7. Schematic illustration of the structure and kinematics of ENAM. Red arrows and blue crosses indicate the orientations of anisotropy. Black arrows indicate previous or current extension, compression, or mantle flow. Brown dikes are illustrated in the lithosphere. Olivine crystals are illustrated with CPO. Red and green dots correspond to the same regions as in Figure 3 and 5. CPO: crystallographic-preferred orientation. AP: Appalachian plains. HA: Harrisonburg Anomaly. COT: continent-ocean transition.

tablished using body-wave tomography, which has less sensitivity to variation in velocity with depth than, for example, receiver functions (*e.g.,* Yuan et al., 2017; Liu & Gao, 2018).

Near the South Georgia Rift (SGR), we observe a shallow, high velocity feature, about 2% fast ($\sim$ 81°W, 33°N, 70 km depth) (Figure 3). This distinctly follows the Brunswick positive magnetic anomaly (BMA) and more subtly follows positive gravity anomalies. Wide-angle seismic results suggest that across the failed Georgia rift, high velocity material intruded the lower crust as part of the Central Atlantic Magmatic Province (CAMP) (Marzen et al., 2020). The imaged fast velocity feature is potentially crustal CAMP underplating, with recovery smeared vertically through the lithosphere according to synthetic tests (Figure S9 and S14). This fast feature extends from the SGR to the continent-ocean transition (COT), and arguably, to some extent, delineates the COT. The connection of the BMA- and SGR-correlated fast velocity anomaly to more fast velocity anomalies delineating the COT suggests that these fast features are of the same cause. Possibly, igneous material from the initial phase of rifting, now solidified, eventually localized from the failed SGR to the COT as part of continental break-up. Alternatively, the fast features near the BMA might be related to an Alleghanian suture (*e.g.,* Lizarralde et al., 1994; Hopper et al., 2016). This fast feature was not clearly resolved in recent mantle tomography models, possibly due to the exclusion of margin-crossing data (*e.g.,* Biryol et al., 2016; Wagner et al., 2018; Savage, 2021).

Our models show laterally complex anisotropy on the continent, above $\sim$ 200 km depth (Figure 4 and 5). Many rifts exhibit extension-perpendicular (rift-parallel) anisotropy (*e.g.,* Vauchez et al., 1998, 2000; Kendall et al., 2005; Eilon et al., 2014). This is in part due to shape-preferred orientation structures such as dike intrusions and melt lenses. However, if extensional strain and consequent CPO dominates anisotropy, then extension parallel splits should be seen (Tommasi et al., 1999). This is indeed observed in some well-developed rifts (Eilon et al., 2014, 2016) and at mid-ocean ridges (Wolfe & Solomon, 1998). We see a mix of margin parallel anisotropy (*i.e.,* approximately parallel to the Appalachians) and margin perpendicular anisotropy (*i.e.* approximately parallel to spreading) near the Piedmont and coastal plains (Figure 4 and 5). This is consistent with Aragon et al. (2017). Extension-induced CPO, now frozen in, may explain the lithospheric extension-parallel anisotropy (*e.g.,* Tommasi et al., 1999). Fossil-melt shape-preferred orientation (SPO) may explain some margin parallel anisotropy. However, igneous SPO at rifts is attributed to the strong velocity contrast between melt and host material (*e.g.,* Kendall et al., 2005). This velocity contrast is strongly reduced once melt solidifies. Igneous SPO is a poor candidate for explaining present-day anisotropy, except perhaps near the HA, where melt may be present.

The Appalachians also exhibit convergence-induced anisotropy that is frozen-in (*e.g.,* Long et al., 2016). Splitting is dominantly margin/orogen parallel at the west border of our anisotropic model, where rift deformation is less prominent (Figure 4). The competing influence of convergence, extension, and possibly igneous SPO can produce the complex lithospheric anisotropy we imaged (Figure 4). Such complexity is further expected from laterally heterogeneous volcanism (*e.g.,* Greene et al., 2020) and extension (*e.g.,* Withjack & Schlische, 2005).

Orthogonal and effectively cancelling anisotropic layers is one proposed explanation for null splitting in portions of the continental coast (Wagner et al., 2012; Long et al., 2016). We imaged variations in anisotropy with depth, and in particular, the transition to margin parallel in the asthenosphere (Figure 5). Depending on the local magnitudes of anisotropic layers, this is capable of causing null splitting. However, our results cannot rule out the contributions of vertical mantle flow to null splitting measurements because we assumed a horizontal symmetry axis.

4.2 Rift-drift transition

4.2.1 Lithospheric structure

Recent work suggests that proto-oceanic crust was emplaced during the transition from rifting to drifting between the East Coast magnetic anomaly (ECMA) and Blake Spur magnetic anomaly (BSMA) (Shuck et al., 2019; Bécel et al., 2020). We observe a shallow, $\sim$ 1.5% slow velocity anomaly above $\sim$ 100 km at the ocean which parallels the ECMA ($\sim$ 74°W, 35°N) (Figure 3). No such feature or trend manifests in the anisotropy model. The gradient in velocity between fast values inboard of the ECMA and slow values seaward of this lineament is suggestive of a relatively rapid contrast in lithospheric thickness (Figure 3, 5, and 7). This is consistent with localized crustal thinning observed by Lynner and Porritt (2017) and Li and Gao (2019). We are hesitant to over-interpret small-scale velocity anomalies beneath the ocean in our models. Synthetic tests indicate that resolution here is relatively poor (Figure S9 and S14). This slow anomaly may reflect persistent continental crust remnant from the rifting process, but that assertion requires further investigation.

There is limited detailed imaging of passive margins at a lithospheric scale to compare our results. In NW Namibia, receiver functions indicate a lithospheric feature that thins from 120 km to 80 km at the COT. Thinned lithosphere at rifted COTs may be a common theme (Figure 7). Because the private African dataset is the only other broadband OBS dataset to cross a rifted passive margin, our results are some of the first detailed mantle-scale seismic models of a rifted COT.

4.2.2 Preserved extensional fabric in transitional-oceanic lithosphere

Globally, anisotropic fast directions within the oceanic lithosphere tend to align with paleo-spreading (*e.g.,* Wolfe & Solomon, 1998; Becker et al., 2014). This supports the notion that upper mantle anisotropy develops parallel to plate motion and is then frozen within the lithosphere. Although the nearby Cretaceous Atlantic lithosphere shows spreading-parallel fast lithospheric anisotropy (Gaherty et al., 2004), splitting measurements offshore at ENAM are instead margin-parallel-fast (Lynner & Bodmer, 2017). This could corroborate many other studies showing mismatch of anisotropy to paleo-spreading and absolute-plate-motion (*e.g.,* Dunn et al., 2005; Takeo et al., 2016; Eilon & Forsyth, 2020).

Synthetic tests (Figure S15) suggest that simple layering is resolved in our models, albeit with reduced amplitudes. We image margin parallel anisotropy in the asthenosphere rather than lithosphere ($> 1\%$ anisotropy beneath ~ 100 km). The asthenospheric anisotropy produces the surprising offshore splitting measurements (Figure 5). Margin parallel flow can explain the asthenospheric anisotropy (Section 4.3).

We imaged approximately paleo-spreading-parallel anisotropy in the offshore lower lithosphere (Figure 4 and 5). This supports that the oceanic lithosphere preserves crystallographic-preferred orientation (CPO) of olivine which developed parallel to mid-ocean ridge spreading (*e.g.,* Becker et al., 2014; Russell et al., 2019). We find this layering persists in our model, independent of regularization scheme or whether we assume no anisotropy beneath 300 km (Figure S4 and S5). Synthetic tests (Figure S10 and S15) demonstrate that this result is robust, though we only expect to resolve heterogeneity beneath ~ 70 km. Above this, it is possible that anisotropy rotates to be paleo-spreading perpendicular (*e.g.,* Shuck & Van Avendonk, 2016).

Offshore ENAM, there are only global seismic models for comparison in the mantle. Although global models are highly variable, they tend to show instead margin perpendicular anisotropy in the asthenosphere and have little consensus in the lithosphere (see compilation of Schaeffer et al., 2016). Our models capture the offshore anisotropic layers ultimately absent in global models, demonstrating the importance of utilizing broadband OBSs to accurately characterize the oceans.

4.3 Active mantle processes at the passive margin

The causes of low velocity anomalies at ENAM, in particular the prominent Harrisonburg anomaly (HA), are subject to debate (*e.g.,* Chu et al., 2013; Mazza et al., 2014). High temperature and possibly partial melt may cause the HA. Savage (2021) estimated up to 2% melt based on the magnitude of their inverted Vs anomaly, and our velocity anomaly is of similar magnitude (about 5% slow). An abrupt increase in attenuation at the HA (Byrnes et al., 2019), high conductivity (Evans et al., 2019), and coincidence with 48 Ma volcanics (Figure 1; Mazza et al., 2014) also suggests the presence of partial melt. The HA is associated with a dynamic topography anomaly, which likely resulted from buoyant mantle (Ramsay & Pysklywec, 2011; Rowley et al., 2013). Receiver functions indicate thinned lithosphere (Evans et al., 2019). Our models add to a preponderance of evidence that there is a present-day mantle upwelling that significantly perturbs the lithosphere beneath Harrisonburg, VA.

Edge-driven convection (EDC) is density-driven flow that is excited by strong lateral gradients in temperature at the edge of cold, continental lithosphere (*e.g.,* King & Ritsema, 2000; Shahnas & Pysklywec, 2004; King, 2007). This process may be important at ENAM (*e.g.,* Ramsay & Pysklywec, 2011; Menke et al., 2016). Some have conjectured that the HA represents the low wavespeed, low density upwelling limb of EDC along the margin (*e.g.,* Savage et al., 2017; Byrnes et al., 2019). Our models are consistent with this theory. Despite relative tectonic quiescence in this region, the HA is the slowest feature in the models, suggesting active processes must maintain a velocity contrast. The presence of well established, high velocity lithosphere beginning ~ 400 km northwest from this feature is consistent with a cold, thick lithospheric edge where the downwelling limbs of convective cells could originate (Figure 5). Unfortunately, anisotropic coverage is limited where we interpret EDC. We are cautious to evaluate EDC mantle flow using the anisotropy model. However, we do not detect strong azimuthal anisotropy at the HA (Figure 5). This is (non-uniquely) consistent with EDC upwelling (*e.g.,* Long et al., 2010). These structures match the geodynamic setting for EDC (*e.g.,* King & Anderson, 1998).

EDC upwellings can occur in laterally isolated cells (Ramsay & Pysklywec, 2011). Our model shows similar, lower amplitude anomalies elsewhere along the margin (Figure 3). The presence of a low velocity anomaly just above the 410 km mantle transition zone, southeast of the HA (Figure 5), may further be associated with EDC. This could result from a convection cell or upwelling feature between the COT and the HA. Some 3-D EDC models might predict similar features (Kaislaniemi & Van Hunen, 2014). Modelling of the analogous African margin (Kaislaniemi & Van Hunen, 2014) also suggests a margin-parallel component of flow is possible with EDC. This could explain some disconnect between the expected margin perpendicular convective flow and anisotropy. The EDC-like low-velocity anomalies imaged here are in addition to the low velocity Georgia anomaly (only peripherally imaged here: Biryol et al., 2016), a low velocity mantle anomaly in Texas (Pollitz & Mooney, 2016), and the Northern Appalachian Anomaly (Menke et al., 2016). EDC is an attractive theory for explaining a variety of discontinuous, short-wavelength, upper mantle velocity features imaged here and elsewhere without invoking multiple processes (Menke et al., 2016).

There are other possible causes of the HA. Although fertile mantle with reduced Mg# can decrease Vs, a reasonable Mg# likely only contributes -1% dVs (Pollitz & Mooney, 2016). Volatiles, possibly originating from the subducted Farallon slab (Van Der Lee et al., 2008), could also reduce velocity. However, velocity reduction is likely less than 3% (Pollitz & Mooney, 2016; Savage, 2021), and the anomaly is at least 5% slow in our models. Plume presence (Chu et al., 2013) may not be supported. We see no low velocity plume track connected to the HA in our results and others (Pollitz & Mooney, 2016), and melting temperatures were too cold (Mazza et al., 2014).

Another frequently invoked geodynamic process beneath ENAM is delamination of the lithosphere. In this scenario, the HA results from asthenospheric return flow (*e.g.,* Mazza et al., 2014; Biryol et al., 2016; Byrnes et al., 2019). Previous delamination may have carved the lithospheric gap and promoted EDC (*e.g.,* Byrnes et al., 2019). Similarly, if a plume did erode the lithosphere, the modified lithospheric topography may have promoted asthenospheric inflow or EDC (Tao et al., 2021).

The increase in lithospheric thickness moving into the craton (the keel) might have an important influence on mantle flow. The keel can redirect horizontally flowing mantle around the continent, producing keel-parallel flow. Some splitting trends in the continent have been attributed to this phenomenon (*e.g.,* Fouch et al., 2000; Yang et al., 2017). Our model shows margin parallel asthenospheric anisotropy well within the continent (Figure 5), consistent with keel-deflected flow. Similarly, we note that a step in the thickness of the lithosphere at the COT could promote margin parallel flow (*e.g.,* Wang & Becker, 2019).

4.3.1 Offshore asthenospheric flow and anisotropy

Density-driven flow may also contribute to margin parallel anisotropy offshore ENAM (Lynner & Bodmer, 2017). Globally, asthenospheric anisotropy beneath the oceans tends to align with plate motion, with maximum match at ~ 200 km depth (Becker et al., 2014). Limited data makes this trend difficult to assess at rifted continent-ocean transitions. In the asthenosphere, our model can resolve the first order anisotropic structure (Figure S15). The model shows instead anisotropy perpendicular to current plate motion and paleo-spreading (Figure 1 and 5).

Plate motion has only a partial control on asthenospheric shear, and inclusion of density-driven flow is needed to explain anisotropy in much of the oceanic asthenosphere (Becker et al., 2014). Density driven flow could help explain oceanic margin-parallel anisotropy seen in the deeper layers of our models (Lynner & Bodmer, 2017). The two layer lithosphere-asthenosphere mantle flow model of Wang and Becker (2019) predicted margin-perpendicular splitting offshore. By adding 3-D flow driven by density anomalies, splitting becomes more margin parallel (Wang & Becker, 2019). Some other density-driven mantle flow models also show approximately margin parallel flow here (*e.g.,* Rowley et al., 2013).

4.4 Relationship between anisotropic fabric and strain

The fast polarization of splitting is usually assumed to indicate modern mantle deformation (*e.g.,* Zhang & Karato, 1995). However, recent experiments have revealed several complexities in mantle CPO development (*e.g.,* Skemer & Hansen, 2016) that require consideration of time-integrated strain patterns (Kaminski & Ribe, 2002). For example, static annealing can modify otherwise steady CPO through time (Boneh et al., 2017). Our model does show some paleo-spreading perpendicular anisotropy in the offshore lithosphere (Figure 4), albeit where resolution is reduced (Figure S9). Since this is nearly 200 ma lithosphere, static annealing may partially account for reoriented CPO.

If CPO is already present, then overprinting fabrics to reflect changed asthenospheric flow can require substantial strain, sometimes up to several hundred percent (Skemer et al., 2012; Boneh & Skemer, 2014; Boneh et al., 2015). For small strain, CPO may be in a transient state and not reflect modern asthenospheric flow in a simple way. CPO may similarly be in a transient state if asthenospheric flow orientation changes over small spatial and temporal scales (Kaminski & Ribe, 2002; Skemer et al., 2012). Anisotropy may not clearly reflect asthenospheric flow in convective systems spanning short distances, or where mantle flow changes through time, such as EDC (*e.g.* Kaislaniemi & Van Hunen, 2014). In the asthenosphere, our anisotropy model shows some heterogeneity at wavelengths down to ~ 100 km (Figure 4). We speculate that flow at this scale might have produced transient state anisotropy with fast orientations not clearly reflecting modern mantle flow. Northwest of the HA, within the asthenosphere, we predict margin-perpendicular EDC to produce margin-perpendicular anisotropy. However, we observe complicated, yet more dominantly margin parallel, anisotropy. This may be a result of transient-state CPO. In contrast, for larger-scale margin parallel asthenospheric flow, particularly beneath the ocean, CPO should reach steady state and produce margin parallel anisotropy. This matches the more strongly margin-parallel asthenospheric anisotropy offshore (Figures 3 and 4).

5 Conclusion

We present S-wave tomography models from a passive broadband dataset spanning the continent-ocean transition of the eastern North American rifted margin (ENAM). Our inversion technique places depth constraints on isotropic and anisotropic structures. It also resolves trade-offs present in single-parameter inversions by simultaneous fitting of travel time and shear wave splitting data. The resultant models provide the first high-resolution images of seismic velocity and azimuthal anisotropy to sub-lithospheric depth across the margin.

Offshore, we find that the rifted continental to oceanic lower lithosphere preserves extension-parallel anisotropy. Onshore, complex lithospheric anisotropy likely reflects the competing effects of extension and convergence over several Wilson cycles. In the asthenosphere, margin parallel anisotropy dominates. This may reflect mantle flow due to density gradients or pressure gradients associated with a step in lithospheric thickness. Isotropic velocities within the continent show the thick, high-velocity continental keel inboard of the Appalachians and the low-velocity Harrisonburg Anomaly associated with Eocene volcanics. This latter feature, together with other small-wavelength velocity anomalies, are consistent with edge-driven convection and other active mantle flow processes at the passive margin.

These results, made possible by an unusual amphibious broadband dataset, demonstrate the dynamic and complex nature of mantle processes at the rifted continent-ocean transition. This study, together with other products of the ENAM-CSE, reinforces the importance of shoreline-crossing instrumentation.

Acknowledgments

We thank Toshiro Tanimoto and Robin Matoza for suggestions which improved the manuscript. All waveform data is available through the IRIS Data Management Center (https://ds.iris.edu/ds/nodes/dmc/). We used network codes TA, YO, CO, ET, N4, PE, SP, SS, XQ, and Z4. Shear-wave splitting from previous literature is available as published supplementary data (Long et al., 2016; Lynner & Bodmer, 2017; Yang et al., 2017). This work was funded by NSF OCE 1753722 and OCE 2001145.

References

Abt, D. L., Fischer, K. M., French, S. W., Ford, H. A., Yuan, H., & Romanowicz, B. (2010). North American lithospheric discontinuity structure imaged by Ps and Sp receiver functions. *Journal of Geophysical Research*, *115*(B9). doi: 10.1029/2009JB006914

Akintunde, O. M., Knapp, C. C., & Knapp, J. H. (2014). Tectonic significance of porosity and permeability regimes in the red beds formations of the South Georgia Rift Basin. *Tectonophysics*, *632*, 1–7. doi: 10.1016/j.tecto.2014.07.029

Aragon, J. C., Long, M. D., & Benoit, M. H. (2017). Lateral Variations in SKS Splitting Across the MAGIC Array, Central Appalachians. *Geochemistry, Geophysics, Geosystems*, *18*(11), 4136–4155. doi: 10.1002/2017GC007169

Bécel, A., Davis, J. K., Shuck, B. D., Van Avendonk, H. J. A., & Gibson, J. C. (2020). Evidence for a Prolonged Continental Breakup resulting from Slow Extension Rates at the Eastern North American Volcanic Rifted Margin. *Journal of Geophysical Research: Solid Earth*, *125*(9), 1–27. doi: 10.1029/2020JB020093

Becker, T. W., Conrad, C. P., Schaeffer, A. J., & Lebedev, S. (2014). Origin of azimuthal seismic anisotropy in oceanic plates and mantle. *Earth and Planetary Science Letters*, *401*(1), 236–250. doi: 10.1016/j.epsl.2014.06.014

Bedle, H., & van der Lee, S. (2009). S velocity variations beneath North America. *Journal of Geophysical Research: Solid Earth*, *114*(B7), 1–22. doi: 10.1029/2008JB005949

Begg, G., Griffin, W., Natapov, L., O'Reilly, S. Y., Grand, S., O'Neill, C., . . . Bowden, P. (2009). The lithospheric architecture of Africa: Seismic tomography, mantle petrology, and tectonic evolution. *Geosphere*, *5*(1), 23–50. doi: 10.1130/GES00179.1

Bezada, M. J., Faccenda, M., & Toomey, D. R. (2016). Representing anisotropic subduction zones with isotropic velocity models: A characterization of the problem and some steps on a possible path forward. *Geochemistry, Geophysics, Geosystems*, *17*(8), 3164–3189. doi: 10.1002/2016GC006507

Biryol, C. B., Wagner, L. S., Fischer, K. M., & Hawman, R. B. (2016). Relationship between observed upper mantle structures and recent tectonic activity across the Southeastern United States. *Journal of Geophysical Research: Solid Earth*, *121*(5), 3393–3414. doi: 10.1002/2015JB012698

Boneh, Y., Morales, L. F., Kaminski, E., & Skemer, P. (2015). Modeling olivine CPO evolution with complex deformation histories: Implications for the interpretation of seismic anisotropy in the mantle. *Geochemistry, Geophysics, Geosystems*, *16*(10), 3436–3455. doi: 10.1002/2015GC005964

Boneh, Y., & Skemer, P. (2014). The effect of deformation history on the evolution of olivine CPO. *Earth and Planetary Science Letters*, *406*, 213–222. doi: 10.1016/j.epsl.2014.09.018

Boneh, Y., Wallis, D., Hansen, L. N., Krawczynski, M. J., & Skemer, P. (2017). Oriented grain growth and modification of 'frozen anisotropy' in the lithospheric mantle. *Earth and Planetary Science Letters*, *474*, 368–374. doi:

10.1016/j.epsl.2017.06.050

Boyd, O. S., Jones, C. H., & Sheehan, A. F. (2004). Foundering lithosphere imaged beneath the southern Sierra Nevada, California, USA. *Science*, *305*(5684), 660–662. doi: 10.1126/science.1099181

Buehler, J. S., & Shearer, P. M. (2017). Uppermost mantle seismic velocity structure beneath USArray. *Journal of Geophysical Research: Solid Earth*, *122*(1), 436–448. doi: 10.1002/2016JB013265

Byrnes, J. S., Bezada, M., Long, M. D., & Benoit, M. H. (2019). Thin lithosphere beneath the central Appalachian Mountains: Constraints from seismic attenuation beneath the MAGIC array. *Earth and Planetary Science Letters*, *519*(1), 297–307. doi: 10.1016/j.epsl.2019.04.045

Chang, S., Ferreira, A. M. G., Ritsema, J., van Heijst, H. J., & Woodhouse, J. H. (2015). Joint inversion for global isotropic and radially anisotropic mantle structure including crustal thickness perturbations. *Journal of Geophysical Research: Solid Earth*, *120*(6), 4278–4300. doi: 10.1002/2014JB011824

Chowns, T. M., & Williams, C. T. (1983). Pre-Cretaceous rocks beneath the Georgia coastal plain—Regional implications. *US Geological Survey Professional Paper*, *1313-A*, 1–42. doi: 10.3133/pp1313

Chu, R., Leng, W., Helmberger, D. V., & Gurnis, M. (2013). Hidden hotspot track beneath the eastern United States. *Nature Geoscience*, *6*, 963–966. doi: 10.1038/ngeo1949

Crosby, A., White, N., Edwards, G., & Shillington, D. J. (2008). Evolution of the Newfoundland–Iberia conjugate rifted margins. *Earth and Planetary Science Letters*, *273*(1-2), 214–226. doi: 10.1016/j.epsl.2008.06.039

DeMets, C., Gordon, R. G., & Argus, D. F. (2010). Geologically current plate motions. *Geophysical Journal International*, *181*(1), 1–80. doi: 10.1111/j.1365-246X.2009.04491.x

Dunn, R. A., Lekić, V., Detrick, R. S., & Toomey, D. R. (2005). Three-dimensional seismic structure of the Mid-Atlantic Ridge (35N): Evidence for focused melt supply and lower crustal dike injection. *Journal of Geophysical Research: Solid Earth*, *110*(B9), 1–17. doi: 10.1029/2004JB003473

Eilon, Z., Abers, G. A., & Gaherty, J. B. (2016). A joint inversion for shear velocity and anisotropy: The Woodlark Rift, Papua New Guinea. *Geophysical Journal International*, *206*(2), 807–824. doi: 10.1093/gji/ggw177

Eilon, Z., Abers, G. A., Gaherty, J. B., & Jin, G. (2015). Imaging continental breakup using teleseismic body waves: The Woodlark Rift, Papua New Guinea. *Geochemistry, Geophysics, Geosystems*, *16*(8), 2529–2548. doi: 10.1002/2015GC005835

Eilon, Z., Abers, G. A., Jin, G., & Gaherty, J. B. (2014). Anisotropy beneath a highly extended continental rift. *Geochemistry, Geophysics, Geosystems*, *15*(3), 545–564. doi: 10.1002/2013GC005092

Eilon, Z. C., & Forsyth, D. W. (2020). Depth-Dependent Azimuthal Anisotropy Beneath the Juan de Fuca Plate System. *Journal of Geophysical Research: Solid Earth*, *125*(8), 1–17. doi: 10.1029/2020JB019477

Evans, R. L., Benoit, M. H., Long, M. D., Elsenbeck, J., Ford, H. A., Zhu, J., & Garcia, X. (2019). Thin lithosphere beneath the central Appalachian Mountains: A combined seismic and magnetotelluric study. *Earth and Planetary Science Letters*, *519*(1), 308–316. doi: 10.1016/j.epsl.2019.04.046

Forte, A. M., Mitrovica, J. X., Moucha, R., Simmons, N. A., & Grand, S. P. (2007). Descent of the ancient Farallon slab drives localized mantle flow below the New Madrid seismic zone. *Geophysical Research Letters*, *34*(4), 1–5. doi: 10.1029/2006GL027895

Fouch, M. J., Fischer, K. M., Parmentier, E. M., Wysession, M. E., & Clarke, T. J. (2000). Shear wave splitting, continental keels, and patterns of mantle flow. *Journal of Geophysical Research: Solid Earth*, *105*(B3), 6255–6275. doi:

10.1029/1999JB900372

Gaherty, J. B., Lizarralde, D., Collins, J. A., Hirth, G., & Kim, S. (2004). Mantle deformation during slow seafloor spreading constrained by observations of seismic anisotropy in the western Atlantic. *Earth and Planetary Science Letters*, *228*(3-4), 255–265. doi: 10.1016/j.epsl.2004.10.026

Golos, E. M., Fang, H., Yao, H., Zhang, H., Burdick, S., Vernon, F., ... van der Hilst, R. D. (2018). Shear Wave Tomography Beneath the United States Using a Joint Inversion of Surface and Body Waves. *Journal of Geophysical Research: Solid Earth*, *123*(6), 5169–5189. doi: 10.1029/2017JB014894

Greene, J. A., Tominaga, M., & Miller, N. C. (2020). Along-Margin Variations in Breakup Volcanism at the Eastern North American Margin. *Journal of Geophysical Research: Solid Earth*, *125*(12), 1–22. doi: 10.1029/2020JB020040

Gripp, A. E., & Gordon, R. G. (2002). Young tracks of hotspots and current plate velocities. *Geophysical Journal International*, *150*(2), 321–361. doi: 10.1046/j.1365-246X.2002.01627.x

Hammond, W. C., & Toomey, D. R. (2003). Seismic velocity anisotropy and heterogeneity beneath the Mantle Electromagnetic and Tomography Experiment (MELT) region of the East Pacific Rise from analysis of P and S body waves. *Journal of Geophysical Research: Solid Earth*, *108*(B4). doi: 10.1029/2002JB001789

Hess, H. H. (1962). History of Ocean Basins. In *Petrologic studies.* Geological Society of America. doi: 10.1130/Petrologic.1962.599

Hopper, E., Fischer, K. M., Rondenay, S., Hawman, R. B., & Wagner, L. S. (2016). Imaging crustal structure beneath the southern Appalachians with wavefield migration. *Geophysical Research Letters*, *43*(23), 12,054–12,062. doi: 10.1002/2016GL071005

Huismans, R., & Beaumont, C. (2011). Depth-dependent extension, two-stage breakup and cratonic underplating at rifted margins. *Nature*, *473*, 74–78. doi: 10.1038/nature09988

Kaislaniemi, L., & Van Hunen, J. (2014). Dynamics of lithospheric thinning and mantle melting by edge-driven convection: Application to Moroccan Atlas mountains. *Geochemistry, Geophysics, Geosystems*, *15*(8), 3175–3189. doi: 10.1002/2014GC005414

Kaminski, É., & Ribe, N. M. (2002). Timescales for the evolution of seismic anisotropy in mantle flow. *Geochemistry, Geophysics, Geosystems*, *3*(1), 1–17. doi: 10.1029/2001GC000222

Karato, S.-i., Jung, H., Katayama, I., & Skemer, P. (2008). Geodynamic Significance of Seismic Anisotropy of the Upper Mantle: New Insights from Laboratory Studies. *Annual Review of Earth and Planetary Sciences*, *36*, 59–95. doi: 10.1146/annurev.earth.36.031207.124120

Karato, S.-i., & Wu, P. (1993). Rheology of the Upper Mantle: A Synthesis. *Science*, *260*(5109), 771–778. doi: 10.1126/science.260.5109.771

Kendall, J.-M., Stuart, G. W., Ebinger, C. J., Bastow, I. D., & Keir, D. (2005). Magma-assisted rifting in Ethiopia. *Nature*, *433*, 146–148. doi: 10.1038/nature03161

Kennett, B. L. N., & Engdahl, E. R. (1991). Traveltimes for global earthquake location and phase identification. *Geophysical Journal International*, *105*(2), 429–465. doi: 10.1111/j.1365-246X.1991.tb06724.x

King, S. D. (2007). Hotspots and edge-driven convection. *Geology*, *35*(3), 223–226. doi: 10.1130/G23291A.1

King, S. D., & Anderson, D. L. (1998). Edge-driven convection. *Earth and Planetary Science Letters*, *160*(3-4), 289–296. doi: 10.1016/S0012-821X(98)00089-2

King, S. D., & Ritsema, J. (2000). African hot spot volcanism: Small-scale convection in the upper mantle beneath cratons. *Science*, *290*(5494), 1137–1140. doi: 10.1126/science.290.5494.1137

Larsen, H. C., Mohn, G., Nirrengarten, M., Sun, Z., Stock, J., Jian, Z., ... Zhong, L. (2018). Rapid transition from continental breakup to igneous oceanic crust in the South China Sea. *Nature Geoscience*, *11*, 782–789. doi: 10.1038/s41561-018-0198-1

Li, C., & Gao, H. (2019). Seismic Characteristics of the Crust and Mantle Lithosphere in the Eastern North American Margin Revealed from Full-wave Ambient Noise Tomography. In *Agu fall meeting abstracts* (pp. T21F–0374).

Liu, L., & Gao, S. S. (2018). Lithospheric layering beneath the contiguous United States constrained by S-to-P receiver functions. *Earth and Planetary Science Letters*, *495*(1), 79–86. doi: 10.1016/j.epsl.2018.05.012

Lizarralde, D., Holbrook, W. S., & Oh, J. (1994). Crustal structure across the Brunswick magnetic anomaly, offshore Georgia, from coincident ocean bottom and multi-channel seismic data. *Journal of Geophysical Research: Solid Earth*, *99*(B11), 21741–21757. doi: 10.1029/94JB01550

Long, M. D., & Becker, T. W. (2010). Mantle dynamics and seismic anisotropy. *Earth and Planetary Science Letters*, *297*(3-4), 341–354. doi: 10.1016/j.epsl.2010.06.036

Long, M. D., Benoit, M. H., Chapman, M. C., & King, S. D. (2010). Upper mantle anisotropy and transition zone thickness beneath southeastern North America and implications for mantle dynamics. *Geochemistry, Geophysics, Geosystems*, *11*(10), 1–22. doi: 10.1029/2010GC003247

Long, M. D., Jackson, K. G., & McNamara, J. F. (2016). SKS splitting beneath Transportable Array stations in eastern North America and the signature of past lithospheric deformation. *Geochemistry, Geophysics, Geosystems*, *17*(1), 2–15. doi: 10.1002/2015GC006088

Lynner, C., & Bodmer, M. (2017). Mantle flow along the eastern North American margin inferred from shear wave splitting. *Geology*, *45*(10), 867–870. doi: 10.1130/G38980.1

Lynner, C., & Porritt, R. W. (2017). Crustal structure across the eastern North American margin from ambient noise tomography. *Geophysical Research Letters*, *44*(13), 6651–6657. doi: 10.1002/2017GL073500

Lynner, C., Van Avendonk, H. J. A., Bécel, A., Christeson, G. L., Dugan, B., Gaherty, J. B., ... Wagner, L. S. (2020). The Eastern North American Margin Community Seismic Experiment: An Amphibious Active- and Passive-Source Dataset. *Seismological Research Letters*, *91*(1), 533–540. doi: 10.1785/0220190142

Marzen, R. E., Shillington, D. J., Lizarralde, D., Knapp, J. H., Heffner, D. M., Davis, J. K., & Harder, S. H. (2020). Limited and localized magmatism in the Central Atlantic Magmatic Province. *Nature Communications*, *11*, 1–8. doi: 10.1038/s41467-020-17193-6

Maupin, V., & Park, J. (2007). Theory and Observations – Wave Propagation in Anisotropic Media. In *Treatise on geophysics* (Vol. 1, pp. 289–321). Elsevier. doi: 10.1016/B978-044452748-6.00007-9

Maus, S., Barckhausen, U., Berkenbosch, H., Bournas, N., Brozena, J., Childers, V., ... Caratori Tontini, F. (2009). EMAG2: A 2-arc min resolution Earth Magnetic Anomaly Grid compiled from satellite, airborne, and marine magnetic measurements. *Geochemistry, Geophysics, Geosystems*, *10*(8). doi: 10.1029/2009GC002471

Mazza, S. E., Gazel, E., Johnson, E. A., Kunk, M. J., McAleer, R., Spotila, J. A., ... Coleman, D. S. (2014). Volcanoes of the passive margin: The youngest magmatic event in eastern North America. *Geology*, *42*(6), 483–486. doi: 10.1130/G35407.1

McKenzie, D. (1978). Some remarks on the development of sedimentary basins. *Earth and Planetary Science Letters*, *40*(1), 25–32. doi: 10.1016/0012-821X(78)90071-7

Menke, W. (2012). *Geophysical Data Analysis: Discrete Inverse Theory* (3rd ed.). Elsevier. doi: 10.1016/C2011-0-69765-0

Menke, W., Skryzalin, P., Levin, V., Harper, T., Darbyshire, F., & Dong, T. (2016). The Northern Appalachian Anomaly: A modern asthenospheric upwelling. *Geophysical Research Letters*, *43*(19), 1–7. doi: 10.1002/2016GL070918

Pollitz, F. F., & Mooney, W. D. (2016). Seismic velocity structure of the crust and shallow mantle of the Central and Eastern United States by seismic surface wave imaging. *Geophysical Research Letters*, *43*(1), 118–126. doi: 10.1002/2015GL066637

Ramsay, T., & Pysklywec, R. (2011). Anomalous bathymetry, 3D edge driven convection, and dynamic topography at the western Atlantic passive margin. *Journal of Geodynamics*, *52*(1), 45–56. doi: 10.1016/j.jog.2010.11.008

Rawlinson, N., & Spakman, W. (2016). On the use of sensitivity tests in seismic tomography. *Geophysical Journal International*, *205*, 1221–1243. doi: 10.1093/gji/ggw084

Rickers, F., Fichtner, A., & Trampert, J. (2013). The Iceland-Jan Mayen plume system and its impact on mantle dynamics in the North Atlantic region: Evidence from full-waveform inversion. *Earth and Planetary Science Letters*, *367*, 39–51. doi: 10.1016/j.epsl.2013.02.022

Rowley, D. B., Forte, A. M., Moucha, R., Mitrovica, J. X., Simmons, N. A., & Grand, S. P. (2013). Dynamic topography change of the Eastern United States since 3 million years ago. *Science*, *340*(6140), 1560–1563. doi: 10.1126/science.1229180

Russell, J. B., Gaherty, J. B., Lin, P. Y. P., Lizarralde, D., Collins, J. A., Hirth, G., & Evans, R. L. (2019). High-Resolution Constraints on Pacific Upper Mantle Petrofabric Inferred From Surface-Wave Anisotropy. *Journal of Geophysical Research: Solid Earth*, *124*, 631–657. doi: 10.1029/2018JB016598

Sandoval, S., Kissling, E., Ansorge, J., & SVEKALAPKO Seismic Tomography working Group. (2004). High-resolution body wave tomography beneath the SVEKALAPKO array - II. Anomalous upper mantle structure beneath the central Baltic Shield. *Geophysical Journal International*, *157*(1), 200–214. doi: 10.1111/j.1365-246X.2004.02131.x

Sandwell, D. T., & Smith, W. H. F. (2009). Global marine gravity from retracked Geosat and ERS-1 altimetry: Ridge segmentation versus spreading rate. *Journal of Geophysical Research: Solid Earth*, *114*(B1). doi: 10.1029/2008JB006008

Savage, B. (2021). Body Wave Speed Structure of Eastern North America. *Geochemistry, Geophysics, Geosystems*, *22*, 1–18. doi: 10.1029/2020GC009002

Savage, B., Covellone, B., & Shen, Y. (2017). Wave speed structure of the eastern North American margin. *Earth and Planetary Science Letters*, *459*, 394–405. doi: 10.1016/j.epsl.2016.11.028

Schaeffer, A. J., Lebedev, S., & Becker, T. W. (2016). Azimuthal seismic anisotropy in the Earth's upper mantle and the thickness of tectonic plates. *Geophysical Journal International*, *207*, 901–933. doi: 10.1093/gji/ggw309

Schlische, R. W. (2003). Progress in Understanding the Structural Geology, Basin Evolution, and Tectonic History of the Eastern North American Rift System. In *The great rift valleys of pangea in eastern north america* (Vol. 1, pp. 21–64). Columbia University Press. doi: 10.7312/leto11162-003

Schmandt, B., & Humphreys, E. (2010). Seismic heterogeneity and small-scale convection in the southern California upper mantle. *Geochemistry, Geophysics, Geosystems*, *11*(5), 1–19. doi: 10.1029/2010GC003042

Schmandt, B., & Lin, F. (2014). P and S wave tomography of the mantle beneath the United States. *Geophysical Research Letters*, *41*(18), 6342–6349. doi: 10.1002/2014GL061231

Shahnas, M. H., & Pysklywec, R. N. (2004). Anomalous topography in the western Atlantic caused by edge-driven convection. *Geophysical Research Letters*, *31*(L18611), 1–5. doi: 10.1029/2004GL020882

Shen, W., & Ritzwoller, M. H. (2016). Crustal and uppermost mantle structure beneath the United States. *Journal of Geophysical Research: Solid Earth*, *121*(6), 4306–4342. doi: 10.1002/2016JB012887

Shillington, D. J., Holbrook, W. S., Van Avendonk, H. J., Tucholke, B. E., Hopper, J. R., Louden, K. E., . . . Nunes, G. T. (2006). Evidence for asymmetric nonvolcanic rifting and slow incipient oceanic accretion from seismic reflection data of the Newfoudland margin. *Journal of Geophysical Research: Solid Earth*, *111*(9). doi: 10.1029/2005JB003981

Shuck, B., & Van Avendonk, H. J. (2016). Evolution of the upper lithosphere in the ENAM area from 3-D wide-angle seismic data. *AGUFM*, T51G–2998S.

Shuck, B. D., Van Avendonk, H. J., & Bécel, A. (2019). The role of mantle melts in the transition from rifting to seafloor spreading offshore eastern North America. *Earth and Planetary Science Letters*, *525*, 115756. doi: 10.1016/j.epsl.2019.115756

Silver, P. G. (1996). Seismic anisotropy beneath the continents: Probing the depths of geology. *Annual Review of Earth and Planetary Sciences*, *24*, 385–432. doi: 10.1146/annurev.earth.24.1.385

Silver, P. G., & Chan, W. W. (1991). Shear wave splitting and subcontinental mantle deformation. *Journal of Geophysical Research*, *96*(B10), 16429–16454. doi: 10.1029/91jb00899

Skemer, P., & Hansen, L. N. (2016). Inferring upper-mantle flow from seismic anisotropy: An experimental perspective. *Tectonophysics*, *668-669*, 1–14. doi: 10.1016/j.tecto.2015.12.003

Skemer, P., Warren, J. M., & Hirth, G. (2012). The influence of deformation history on the interpretation of seismic anisotropy. *Geochemistry, Geophysics, Geosystems*, *13*(3), 1–10. doi: 10.1029/2011GC003988

Takeo, A., Kawakatsu, H., Isse, T., Nishida, K., Sugioka, H., Ito, A., . . . Suetsugu, D. (2016). Seismic azimuthal anisotropy in the oceanic lithosphere and asthenosphere from broadband surface wave analysis of OBS array records at 60 Ma seafloor. *Journal of Geophysical Research: Solid Earth*, *121*(3), 1927–1947. doi: 10.1002/2015JB012429

Tao, Z., Li, A., & Fischer, K. M. (2021). Hotspot signatures at the North American passive margin. *Geology*, *49*(5), 525–530. doi: 10.1130/G47994.1

Tommasi, A., Tikoff, B., & Vauchez, A. (1999). Upper mantle tectonics: three-dimensional deformation, olivine crystallographic fabrics and seismic properties. *Earth and Planetary Science Letters*, *168*(1-2), 173–186. doi: 10.1016/S0012-821X(99)00046-1

Van Avendonk, H. J. A., Holbrook, W. S., Nunes, G. T., Shillington, D. J., Tucholke, B. E., Louden, K. E., . . . Hopper, J. R. (2006). Seismic velocity structure of the rifted margin of the eastern Grand Banks of Newfoundland, Canada. *Journal of Geophysical Research: Solid Earth*, *111*(B11404), 1–26. doi: 10.1029/2005JB004156

Van Der Lee, S., Regenauer-Lieb, K., & Yuen, D. A. (2008). The role of water in connecting past and future episodes of subduction. *Earth and Planetary Science Letters*, *273*(1-2), 15–27. doi: 10.1016/j.epsl.2008.04.041

VanDecar, J. C., & Crosson, R. S. (1990). Determination of teleseismic relative phase arrival times using multi-channel cross-correlation and least squares. *Bulletin of the Seismological Society of America*, *80*(1), 150–169.

Vauchez, A., Tommasi, A., & Barruol, G. (1998). Rheological heterogeneity, mechanical anisotropy and deformation of the continental lithosphere. *Tectonophysics*, *296*(1-2), 61–86. doi: 10.1016/S0040-1951(98)00137-1

Vauchez, A., Tommasi, A., Barruol, G., & Maumus, J. (2000). Upper mantle deformation and seismic anisotropy in continental rifts. *Physics and Chemistry* *of the Earth, Part A: Solid Earth and Geodesy*, *25*(2), 111–117. doi: 10.1016/S1464-1895(00)00019-3

Vine, F. J., & Mathews, D. H. (1963). Magnetic Anomalies Over Oceanic Ridges. *Nature*, *199*(4897), 947–949. doi: 10.1038/199947a0

Wagner, L. S., Fischer, K. M., Hawman, R., Hopper, E., & Howell, D. (2018). The relative roles of inheritance and long-term passive margin lithospheric evolution on the modern structure and tectonic activity in the southeastern United States. *Geosphere*, *14*(4), 1385–1410. doi: 10.1130/GES01593.1

Wagner, L. S., Long, M. D., Johnston, M. D., & Benoit, M. H. (2012). Lithospheric and asthenospheric contributions to shear-wave splitting observations in the southeastern United States. *Earth and Planetary Science Letters*, *341-344*, 128–138. doi: 10.1016/j.epsl.2012.06.020

Wang, H., Zhao, D., Huang, Z., & Wang, L. (2019). Tomography, Seismotectonics, and Mantle Dynamics of Central and Eastern United States. *Journal of Geophysical Research: Solid Earth*, *124*(8), 8890–8907. doi: 10.1029/2019JB017478

Wang, W., & Becker, T. W. (2019). Upper mantle seismic anisotropy as a constraint for mantle flow and continental dynamics of the North American plate. *Earth and Planetary Science Letters*, *514*(May), 143–155. doi: 10.1016/j.epsl.2019.03.019

Wernicke, B. (1985). Uniform-sense normal simple shear of the continental lithosphere. *Canadian Journal of Earth Sciences*, *22*(1), 108–125. doi: 10.1139/e85-009

Withjack, M. O., & Schlische, R. W. (2005). A Review of Tectonic Events on the Passive Margin of Eastern North America. In *Petroleum systems of divergent continental margin basins* (pp. 203–235). SEPM Society for Sedimentary Geology. doi: 10.5724/gcs.05.25.0203

Withjack, M. O., Schlische, R. W., & Olsen, P. E. (2012). Development of the passive margin of Eastern North America: Mesozoic Rifting, Igneous Activity, and Breakup. In *Regional geology and tectonics: Phanerozoic rift systems and sedimentary basins* (pp. 301–335). Elsevier. doi: 10.1016/B978-0-444-56356-9.00012-2

Wolfe, C. J., & Solomon, S. C. (1998). Shear-Wave Splitting and Implications for Mantle Flow Beneath the MELT Region of the East Pacific Rise. *Science*, *280*(5367), 1230–1232. doi: 10.1126/science.280.5367.1230

Worthington, L., Shuck, B., Becel, A., Eilon, Z., & Lynner, C. (2021, mar). Breaking Up Is Hard to Do, Especially for Continents. *Eos*, *102*. doi: 10.1029/2021EO155889

Yang, B. B., Liu, Y., Dahm, H., Liu, K. H., & Gao, S. S. (2017). Seismic azimuthal anisotropy beneath the eastern United States and its geodynamic implications. *Geophysical Research Letters*, *44*(6), 2670–2678. doi: 10.1002/2016GL071227

Yuan, H., Romanowicz, B., Fischer, K. M., & Abt, D. (2011). 3-D shear wave radially and azimuthally anisotropic velocity model of the North American upper mantle. *Geophysical Journal International*, *184*(3), 1237–1260. doi: 10.1111/j.1365-246X.2010.04901.x

Yuan, X., Heit, B., Brune, S., Steinberger, B., Geissler, W. H., Jokat, W., & Weber, M. (2017). Seismic structure of the lithosphere beneath NW Namibia: Impact of the Tristan da Cunha mantle plume. *Geochemistry, Geophysics, Geosystems*, *18*(1), 125–141. doi: 10.1002/2016GC006645

Zelt, C. A. (1998). Lateral velocity resolution from three-dimensional seismic refraction data. *Geophysical Journal International*, *135*(3), 1101–1112. doi: 10.1046/j.1365-246X.1998.00695.x

Zhang, S., & Karato, S.-i. (1995). Lattice preferred orientation of olivine aggregates deformed in simple shear. *Nature*, *375*(6534), 774–777. doi: 10.1038/375774a0

Ziegler, P. A., & Cloetingh, S. (2004). Dynamic processes controlling evolution of rifted basins. *Earth-Science Reviews*, *64*, 1–50. doi: 10.1016/S0012-8252(03)00041-2

Mantle structure and flow across the continent-ocean transition of the eastern North American margin: anisotropic S-wave tomography

Brennan R. Brunsvik[1 *], Zachary C. Eilon[1], Colton Lynner[2]

[1]Department of Earth Science, University of California, Santa Barbara, CA, USA

[2]Department of Earth Science, University of Delaware, Newark, DE, USA

Contents of this file

1. Sections S1 to S7. Section S1: Multi-channel cross-correlation. Section S1.1: Delay time datasets, processing, and quality control. Section S1.2: Dependence of MCCC on particle motion polarization. Section S2: Tomography parameterization. Section S3: Crustal corrections and static terms. Section S4: Finite frequency approximation. Section S5: Regularization. Section S6: Spike test. Section S7: Squeezing test.

2. Figures S1 to S16. Figure S1: Comparison of shear-wave splitting fast polarizations to assumed anisotropic geometry. Figure S2: Crustal corrections for splitting and differential travel times. Figure S3: L-tests for regularization parameters. Figure S4: Depth-slice

---

*Department of Earth Science, Webb Hall, University of California, Santa Barbara, CA 93106

of model where anisotropy is permitted at all depths. Figure S5: Cross-section of model where anisotropy is permitted at all depths. Figure S6: Synthetic splitting example showing split and splitting corrected waveforms and transverse energy surface. Figure S7: Multi-channel cross-correlation example, showing pre- and post-corrected waveforms and particle motion. Figure S8: Splitting and differential travel times averaged at each station. Figure S9: Velocity checkerboard tests. Figure S10: Anisotropy checkerboard tests. Figure S11: Velocity spike test. Figure S12: Anisotropy spike test. Figure S13: Squeezing test. Figure S14: Synthetic input-output test evaluating specific velocity features. Figure S15: Synthetic input-output test evaluating specific anisotropy features. Figure S16: Velocity and anisotropy models in 3-D.

Additional Supporting Information (Files uploaded separately)

1. Description of interactive tomography model file `brunsvik-tomog.html`

Introduction

This supporting document contains details and figures regarding multi-channel cross-correlation and tomography, as well as tests for resolution, regularization, and for synthetic splitting predictions using a ray-based approach. We included an interactive tomography model figure as `brunsvik-tomog.html`.

S1. Multi-channel cross-correlation

We used multi-channel cross-correlation (MCCC) to measure splitting and differential travel times (VanDecar & Crosson, 1990). Traditionally, travel time differences between each pair of stations are measured through cross-correlation to produce the data vector $\mathbf{d}$. These delay times constitute the model vector $\mathbf{m}$, which are self-consistent differential travel times we seek. These vectors are linearly related through $\mathbf{Gm} = \mathbf{d}$. Differential travel times are inverted using weighted least squares. The additional steps we employ to jointly measure splitting with differential travel times is described in Section 2.1 and Eilon, Abers, and Gaherty (2016).

S1.1. Delay time datasets, processing, and quality control

The seismic array we use has a total aperture of ~ 1500 km east-west and ~ 1000 km north-south. We used shear-wave arrivals from earthquakes between 30° and 151°. We used a distance-dependent M_W cutoff to select events for processing. The minimum M_W cutoff varies linearly between $M_W > 5.5$ at a distance of 30° to $M_W > 6.5$ for events at 135° (*e.g.,* Liu & Gao, 2018). This gives 2326 candidate earthquakes.

We collected splitting and differential travel time datasets from a combination of novel measurements and previously published data. First, we measured differential travel times and splitting times at all stations in our meta-array. We retained splitting times in the coastal region, but discarded these and used only the differential travel times over a wider region (Figure S1 and 2). In addition to this dataset, we processed OBSs a second time, primarily to reduce sparsity of OBS data. For this second dataset, we did not reject waveforms automatically. We manually inspected and considered all waveforms to ensure that signals with good quality were not rejected. Still, due to a shorter deployment interval and a noisier station environment, we obtained fewer travel time and splitting measurements at offshore stations than onshore. To account for this difference in data power within the inversion, we upweighted all OBS measurements by a compensating factor (3x) in the tomography. Third, we incorporated *SK(K)S-PKS* splitting measurements from the literature in our anisotropic region (Figure 1), which were measured using standard splitting techniques (Long et al., 2016; Lynner & Bodmer, 2017; Yang et al., 2017).

We applied the following quality control and data processing prior to MCCC inversions. We removed instrument responses and rotated OBSs to north and east using instrument orientations measured from surface wave polarizations (Lynner & Bodmer, 2017). We rejected body wave arrivals with signal-to-noise ratios less than 2.8 for land stations or 2 for OBSs. We removed phase arrivals which had less than $\sim$ 10 s of separation from another phase. For arrivals with strongly non-linear particle motion, we found our splitting measurements unreliable. Elliptical particle motion for one earthquake's phase arrival, stacked across the array, could also indicate strong source-side splitting. We excluded earthquakes with particle motion ellipticity on the stacked waveform > 0.33. We chose this number by visually inspecting the splitting corrected waveforms for quality, in particular, the similarity and alignment of the splitting corrected S-pulses. We defined ellipticity as the ratio of minimum to maximum eigenvalues of the horizontal particle motion covariance matrix (*e.g.,* Silver & Chan, 1991). We applied a Butterworth band pass filter with high- and low-pass frequencies hand-selected for each earthquake to maximize clarity of the pulse while retaining high frequency energy. The average low- and high-pass frequencies were 0.129 Hz and 0.031 Hz, respectively. After applying MCCC, we rejected measurements which exhibited cycle skipping, had a cross-correlation coefficient with the waveform stack of less than 0.55 for land stations or 0.4 for OBSs, or had increased ellipticity of particle motion. We also rejected waveforms with visually dissimilar pulse shapes or which maintained misalignment of the pulses after applying MCCC.

S1.2. Dependence of MCCC on particle motion polarization

The occurrence of detectable splitting depends on the particle motion polarization relative to the anisotropic symmetry axis. We assume a symmetry axis parallel to $\phi =$ N33°E.

Where particle motion is parallel or perpendicular to ϕ, we expect no splitting. For S-wave arrivals with mean polarization measured to be within 22.5° of ϕ, we used the standard MCCC process to measure only $\delta T_{\parallel}$, the differential travel times at all stations for quasi-S waves polarized parallel to the margin. Similarly, for S-wave arrivals with mean polarization measured to be less than 22.5° from the perpendicular to ϕ, we measured only $\delta T_{\perp}$. Where particle motion polarization is between 22.5° and 67.5° from ϕ, splitting may occur. In this case, we used cross-correlation between each station pair allowing us to measure both $\delta T_{\perp}$ and $\delta T_{\parallel}$. At each individual station, we cross-correlated the margin-parallel and margin-perpendicular horizontal components to measure the splitting times dT_{splt} at each station (Eilon et al., 2016). The resulting quasi-shear wave splitting and differential travel times become the data inputs for our tomographic inversion.

S2. Tomography parameterization

We followed the methodology of Eilon et al. (2016) in applying several key assumptions to reduce the number of independent elastic tensor parameters to two. First, we assume a hexagonal elastic tensor with horizontal symmetry axis of fixed orientation throughout the model to simplify the elastic tensor to 5 independent parameters from 23 (21 elastic and 2 orientation parameters). As noted in Section 2.2, the fixed symmetry axis is not equivalent to assuming a fixed fast orientation, and the assumption is justified by observations of simple splitting from SKS data. Under this parameterization, a shear wave with vertical incidence is already fully described by $V_{\parallel}$ and $V_{\perp}$. By assuming that the anisotropic parameter $\eta = 1$, $V_{P_{av}} = \nu V_{S_{av}}$ where $\nu = 1.8$, and that P and S anisotropy are equal, the elastic tensor can be parameterized as a function of only two values, $V_{\parallel}$ and $V_{\perp}$, for arbitrarily incident rays.

For a ray propagating at an angle ζ to the horizontal hexagonal symmetry axis, the two quasi-shear wave velocities that result from the Christoffel equations are V_{SH} and V_{SV}. V_{SH} is always perpendicular to the hexagonal symmetry axis and is precisely calculable on the basis of $V_{\parallel}$ and $V_{\perp}$. V_{SV} is more complex. We assume the V_{SV} wave is polarized in the vertical plane, which contains the ray propagation path (Eilon et al., 2016). The wavespeed, V_{SV}, is then approximated by a function varying symmetrically about $\zeta = 45°$ between 0° and 90°. The error associated with this assumption is small and discussed in Eilon et al. (2016). The quasi-shear wave velocities are thus:

$$V_{SH}(\zeta) = \sqrt{V_{\perp}^2 \sin^2 \zeta + V_{\parallel}^2 \cos^2 \zeta}$$

$$V_{SV}(\zeta) \approx \sqrt{V_{\parallel}^2 \cos^2 2\zeta + \left(\nu^2 \left[V_{\parallel}^2 - V_{\perp}^2\right]/4 + V_{\parallel}^2\right) \sin^2 2\zeta}$$

Based on our assumptions, Vsh and Vsv correspond directly to the two split quasi-S wave velocities. This paramaterization achieves two key goals: 1) The assumption of fixed symmetry axis makes the splitting process straightforwardly additive (rather than strongly non-commutative). 2) These expressions allow for analytical differentiation of delay times with respect to model parameters. This enables efficient utilization of Newton's method to solve the non-linear inversion.

S3. Crustal corrections and static terms

The relationship between data and model involves integrating slowness through the model, accounting for event and station static terms, and applying a crustal correction. The model is $\mathbf{m} = \left\{\mathbf{V}_{\perp}, \mathbf{V}_{\parallel}, \delta\mathbf{T}_{\mathrm{evt}}, \delta\mathbf{T}_{\mathrm{sta}}, \mathbf{dT}_{\mathrm{evt}}, \mathbf{dT}_{\mathrm{sta}}\right\}$ which is related to data as $\mathbf{d} = g\left(\mathbf{m}\right) + \delta\mathbf{T}_{crust}$ (these terms are defined below) (Eilon et al., 2016). Note that the symbol δ corresponds to isotropic travel times and d to splitting times.

We applied *a priori* crustal corrections $\delta\mathbf{T}_{\mathrm{crust}}$ to account for the influence of known crustal heterogeneity on delay times (Figure S2; *e.g.,* Sandoval et al., 2004). We remove the travel times which deviate from those of a mean crust with thickness $h = 39$ km and $Vs = 3.5$ km/s. We adjust arrival times of all stations to account for elevation, correcting to sea level. We use the crustal velocity and depth model of Shen and Ritzwoller (2016) for the continental crust and Shuck, Van Avendonk, and Bécel (2019) for the oceanic crust. The crustal corrections, ray-averaged at each station, can be seen in Figure S2.

Shallow structure is not formally resolvable using body wave tomography, given the average station spacing of about 70 km. To account for error in *a priori* crustal correction terms, or stations for which crustal values are not independently constrained, we also solved for damped station static travel time terms $\delta\mathbf{T}_{\mathrm{sta}}$ and event travel time terms $\delta\mathbf{T}_{\mathrm{evt}}$. Direct S phase source splitting can be several seconds and contaminate our anisotropy model. This is solved for as event splitting static terms $\mathbf{dT}_{\mathrm{evt}}$. Source-side splitting is thus parsed out separately from splitting in the mantle anisotropy model. Station static splitting terms $\mathbf{dT}_{\mathrm{sta}}$ account for anisotropy that is too shallow to resolve in the main model.

S4. Finite frequency approximation

We account for finite frequency effects using simplified, ray-based kernels (Schmandt & Humphreys, 2010). First, we conduct ray tracing using the reference IASP91 1-D velocity model (Kennett & Engdahl, 1991). Each travel time was calculated using $\delta t = \iiint_{\oplus} K(\mathbf{x})/\delta v\,(\mathbf{x})\,d^3\mathbf{x}$ where $K(\mathbf{x})$ is the sensitivity kernel and δv is the perturbational velocity (δv depends on anisotropy as described in Section S2). We use a modified version of Eq. 2 from Schmandt and Humphreys (2010) to approximate the sensitivity kernel

$K(\mathbf{x})$, ignoring the region outside the first Fresnel zone:

$$K(R_N) \approx A \frac{\sin\left(\pi\left(\frac{R_N}{R_{F_1}(D_R, D_{Rmax}, f_c)}\right)^2\right)}{\int_0^{R_N}\int_0^{2\pi}\sin\left(\pi\left(\frac{R_N}{R_{F_1}(D_R, D_{Rmax}, f_c)}\right)^2\right)d\theta dR_N} \tag{1}$$

where R_N is the ray-normal distance, R_{F_1} is the first Fresnel zone radius, D_R is along-ray distance, D_{Rmax} is the total ray length, and f_c is the center frequency used when cross-correlating waveforms. The denominator involves an integral in the plane normal to the ray. For a given ray, the denominator varies only as a function of D_R. The denominator scales the sensitivity along D_R to account for increase in R_{F_1} with D_R.

Similar to Schmandt and Humphreys (2010), we calculate A by assuming equivalence of travel time sensitivity using both ray and finite frequency approaches: $\iiint_{\oplus} K(\mathbf{x})/v_{ref}(\mathbf{x})d^3\mathbf{x} = \int \frac{1}{v_{ref}(D_R)}dD_R$ where v_{ref} is the 1-D reference velocity. For calculating A, we only perform the integrals in the volume and along the ray corresponding to the portion of the ray where R_{F1} is contained completely within our model.

We approximate the first fresnel zone radius by assuming that all energy is contained at the center frequency f_c and that ray bending is insignificant. Then, the first Fresnel zone (*i.e.* the ray normal distance such that a reflector will cause a ray to arrive at a station with π phase lag compared to the direct ray) is:

$$R_{F_1} \approx \sqrt{\frac{v}{f_c}\frac{D_R\left(D_{Rmax} - D_R\right)}{D_{Rmax}}} \tag{2}$$

S5. Regularization

We conducted L-tests, which aid in determining the optimal model length penalty weight (ϵ) and second derivative roughness penalty weight (γ). We grid searched possible values of ϵ and γ and chose $\epsilon = 22$ and $\gamma = 4.2$ to minimize a regularization penalty function

$P(\epsilon, \gamma)$ (Figure S3). P is a linear combination of roughness, model norm, and data residual. We gave relative penalty weights to model length $\|\mathbf{m}(\epsilon, \gamma)\|$ and roughness $\|\mathbf{m}''(\epsilon, \gamma)\|$ using

$$A = (1 - 0.2)\|\mathbf{m}\| + 0.2\|\mathbf{m}''\|$$

We accounted for data misfit using

$$B = 1 - \mathrm{vr_w}$$

where $\mathrm{vr_w}$ is weighted variance reduction. Then, we calculated the final penalty as

$$P = (1 - 0.35)\left(\frac{A - min(A)}{max(A) - min(A)}\right) + 0.35\left(\frac{B - min(B)}{max(B) - min(B)}\right)$$

We also evaluated P when considering independently the splitting times/anisotropy model, or the differential travel times/isotropic velocity model (not reported here for brevity). We accordingly decreased anisotropy damping by 25% and increased anisotropy smoothing by 150% relative to velocity.

S6. Spike tests

Spike tests (Figure S11 and S12) indicate resolution and have a valuable mathematical meaning (Rawlinson & Spakman, 2016). They provide insight into the model resolution matrix, **R**, whose rows can be thought of as the impulse response function of the inversion (Menke, 2012). Each row of **R** thus indicates the influence of one "true" model parameter on each inverted model parameter. Because it is often computationally infeasible to calculate the full resolution matrix, a spike test – using an input model that is zero at all nodes except for node i – is often used as a proxy for row i of **R**. Note that in practice we must use a box-car or small spherical input rather than a true delta spike (*e.g.,* Rickers et al., 2013). The results of this test are described in Section 3.2.

S7. Squeezing test

We conducted a squeezing test to assess the depth extent which the data require significant velocity heterogeneity and anisotropy. We ran the tomographic inversion with the constraint that dVs and anisotropy are 0 beneath some squeezing depth, z_{sqz} (Figure S13). We varied this squeezing depth parameter, evaluating how variance reduction and model norm changed as a quantitative metric for the depth range over which our data *require* model structure. Variance reduction of delay times is a metric for consistency of the model with the data. Note that differential travel times correspond primarily to isotropic velocity, and splitting times correspond to anisotropy.

Differential travel time variance reduction continues to increase significantly as the squeezing depth increases, to $z_{sqz} \geq 1080$km. This suggests the data require velocity heterogeneity to the 1080 km base of the model. Previous body wave tomography models suggest that structures associated with delamination, convection, sinking slabs, or other processes extend to similar depths (*e.g.,* Golos et al., 2018). Since our focus is on tectonics and mantle-plate dynamics, we do not interpret structures deeper than 660 km.

Splitting time variance reduction continues to increase as z_{sqz} increases. However, this gradient is modest. This suggests the splitting data do not strictly require deep structure. However, the anisotropy model norm increases with increasing z_{sqz}. With unsqueezed anisotropy, deep anisotropy magnitude matches shallow anisotropy magnitude (Figure S4 and S5). We interpret that splitting measurement error is mapped toward the base of the model if not squeezed. Differential travel measurements will also be partially mapped to the deep anisotropy model due to trade-off between anisotropy and velocity. The squeezing test corroborates our decision to permanently squeeze the anisotropy model to what we *a priori* believe is the maximum likely anisotropy depth: 300 km (Chang et al., 2015).

File brunsvik-tomog.html Three dimensional view of anisotropy and velocity model; same as Figure S16. dVs isosurfaces are at $\pm 1.2\%, \pm 2.2\%$. Anisotropy isosurfaces are at $\pm 0.5\%, \pm 1.0\%$. Model only plotted where hit quality > 0.7. Moho adapted from Shen and Ritzwoller (2016) and Shuck et al. (2019). Simply open this file in a web browser to view. Turn on and off different layers (anisotropy, velocity, Moho, and topography) by clicking on their labels.

References

Chang, S., Ferreira, A. M. G., Ritsema, J., van Heijst, H. J., & Woodhouse, J. H. (2015). Joint inversion for global isotropic and radially anisotropic mantle structure including crustal thickness perturbations. *Journal of Geophysical Research: Solid Earth*, *120*(6), 4278–4300. doi: 10.1002/2014JB011824

Eilon, Z., Abers, G. A., & Gaherty, J. B. (2016). A joint inversion for shear velocity and anisotropy: The Woodlark Rift, Papua New Guinea. *Geophysical Journal International*, *206*(2), 807–824. doi: 10.1093/gji/ggw177

Golos, E. M., Fang, H., Yao, H., Zhang, H., Burdick, S., Vernon, F., ... van der Hilst, R. D. (2018). Shear Wave Tomography Beneath the United States Using a Joint Inversion of Surface and Body Waves. *Journal of Geophysical Research: Solid Earth*, *123*(6), 5169–5189. doi: 10.1029/2017JB014894

Kennett, B. L. N., & Engdahl, E. R. (1991). Traveltimes for global earthquake location and phase identification. *Geophysical Journal International*, *105*(2), 429–465. doi: 10.1111/j.1365-246X.1991.tb06724.x

Liu, L., & Gao, S. S. (2018). Lithospheric layering beneath the contiguous United States constrained by S-to-P receiver functions. *Earth and Planetary Science Letters*, *495*(1), 79–86. doi: 10.1016/j.epsl.2018.05.012

Long, M. D., Jackson, K. G., & McNamara, J. F. (2016). SKS splitting beneath Transportable Array stations in eastern North America and the signature of past lithospheric deformation. *Geochemistry, Geophysics, Geosystems*, *17*(1), 2–15. doi: 10.1002/2015GC006088

Lynner, C., & Bodmer, M. (2017). Mantle flow along the eastern North American margin inferred from shear wave splitting. *Geology*, *45*(10), 867–870. doi: 10.1130/G38980.1

Menke, W. (2012). *Geophysical Data Analysis: Discrete Inverse Theory* (3rd ed.). Elsevier. doi: 10.1016/C2011-0-69765-0

Rawlinson, N., & Spakman, W. (2016). On the use of sensitivity tests in seismic tomography. *Geophysical Journal International*, *205*, 1221–1243. doi: 10.1093/gji/ggw084

Rickers, F., Fichtner, A., & Trampert, J. (2013). The Iceland-Jan Mayen plume system and its impact on mantle dynamics in the North Atlantic region: Evidence from full-waveform inversion. *Earth and Planetary Science Letters*, *367*, 39–51. doi: 10.1016/j.epsl.2013.02.022

Sandoval, S., Kissling, E., Ansorge, J., & SVEKALAPKO Seismic Tomography working Group. (2004). High-resolution body wave tomography beneath the SVEKALAPKO array - II. Anomalous upper mantle structure beneath the central Baltic Shield. *Geophysical Journal International*, *157*(1), 200–214. doi: 10.1111/j.1365-246X.2004.02131.x

Schmandt, B., & Humphreys, E. (2010). Seismic heterogeneity and small-scale convection in the southern California upper mantle. *Geochemistry, Geophysics, Geosystems*, *11*(5), 1–19. doi: 10.1029/2010GC003042

Shen, W., & Ritzwoller, M. H. (2016). Crustal and uppermost mantle structure beneath the United States. *Journal of Geophysical Research: Solid Earth*, *121*(6), 4306–4342. doi: 10.1002/2016JB012887

Shuck, B. D., Van Avendonk, H. J., & Bécel, A. (2019). The role of mantle melts in the transition from rifting to seafloor spreading offshore eastern North America. *Earth and Planetary Science Letters*, *525*, 115756. doi: 10.1016/j.epsl.2019.115756

Silver, P. G., & Chan, W. W. (1991). Shear wave splitting and subcontinental mantle deformation. *Journal of Geophysical Research*, *96*(B10), 16429–16454. doi: 10.1029/91jb00899

VanDecar, J. C., & Crosson, R. S. (1990). Determination of teleseismic relative phase arrival times using multi-channel cross-correlation and least squares. *Bulletin of the Seismological Society of America*, *80*(1), 150–169.

Yang, B. B., Liu, Y., Dahm, H., Liu, K. H., & Gao, S. S. (2017). Seismic azimuthal anisotropy beneath the eastern United States and its geodynamic implications. *Geophysical Research Letters*, *44*(6), 2670–2678. doi: 10.1002/2016GL071227

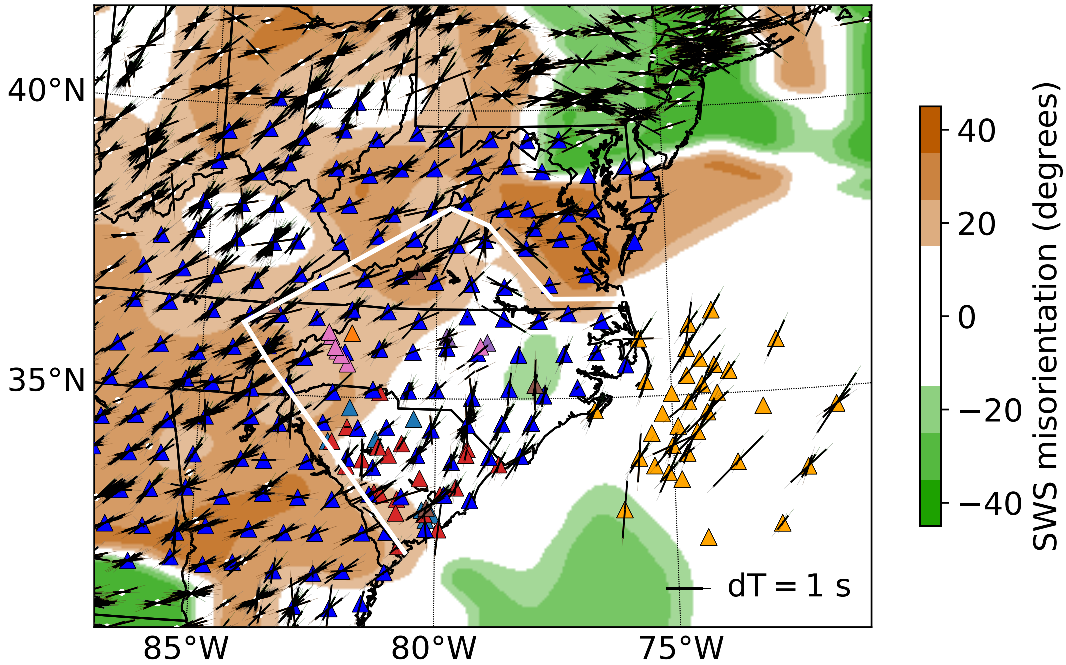

Figure S1. This shows the stations we use (triangles) and previous splitting measurements. The 30 OBSs and 3 land stations that were deployed as part of the ENAM-CSE are shown in orange. Dark blue triangles are the Transportable Array (TA). Other triangles are other networks. The white line shows the boundary between stations used for splitting and stations used only for delay times. Splitting delay times and orientations at OBSs (Lynner & Bodmer, 2017) and land stations (Long et al., 2016; Yang et al., 2017) are shown as black lines. Colors and contours illustrate mismatch between splitting measurements from the literature and the best matching quasi-S wave polarization predicted from our assumed hexagonal symmetry axis orientation (*i.e.* N33°E +n90°). The mismatch thus varies only between −45° and 45° as it is equally acceptable for fast axes to be parallel or perpendicular to the symmetry axis, but our assumptions break down for mismatch of 45°. This mismatch is interpolated onto a grid using a Gaussian filter. A white contour is drawn roughly at 25° mismatch, which we use to limit the bounds of stations used for measuring splitting. OBS: ocean-bottom seismometer. ENAM-CSE: Eastern North American margin community seismic experiment.

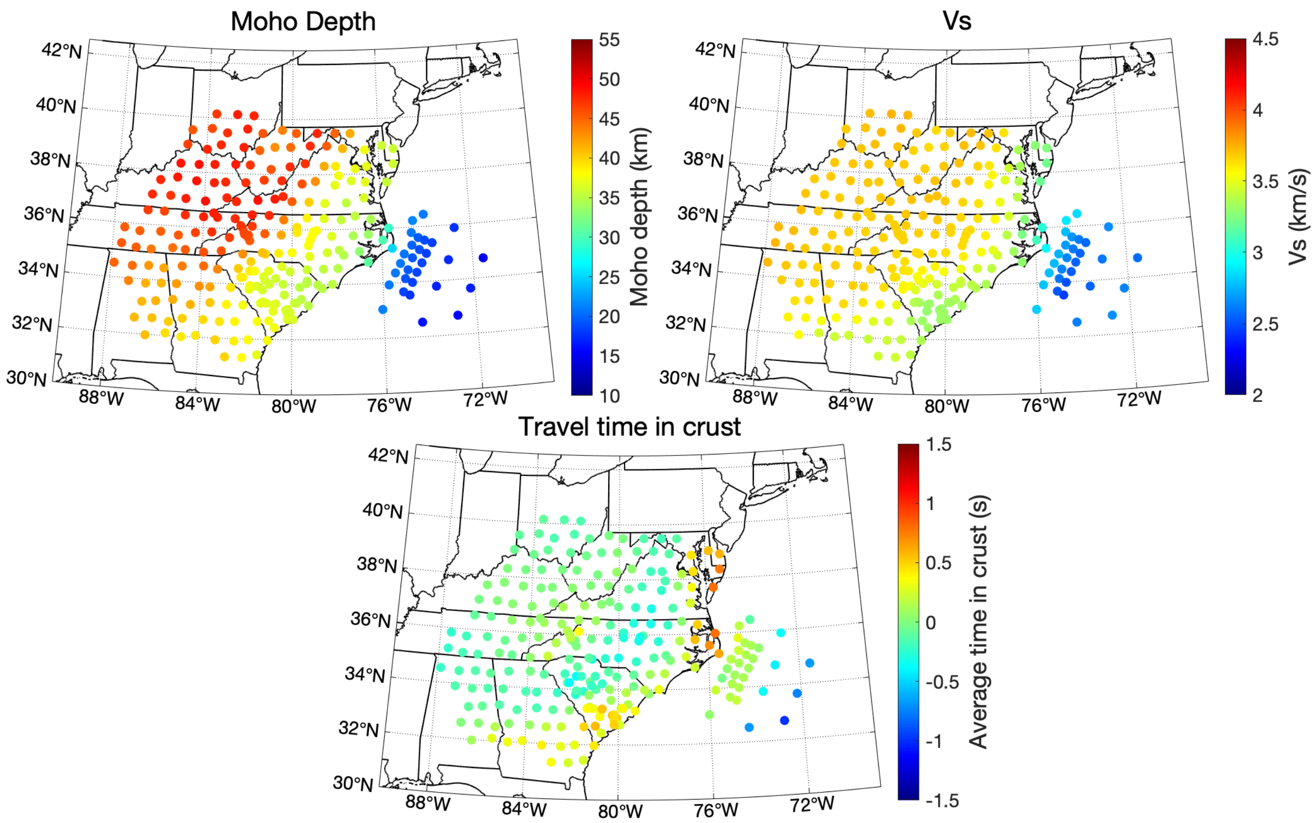

Figure S2. Crustal values and corrections which are applied to the differential travel time data. Top left shows Moho depth and right shows crustal velocity, which is used to calculate crustal corrections. The velocity and Moho profiles of Shen and Ritzwoller (2016) and Shuck et al. (2019) are used for the continental and oceanic crust, respectively. Bottom shows calculated crustal travel time in excess of what would be spent in a laterally homogenous crust. The plots show averages at each station. These values are *removed* from differential travel times to perform the crustal correction.

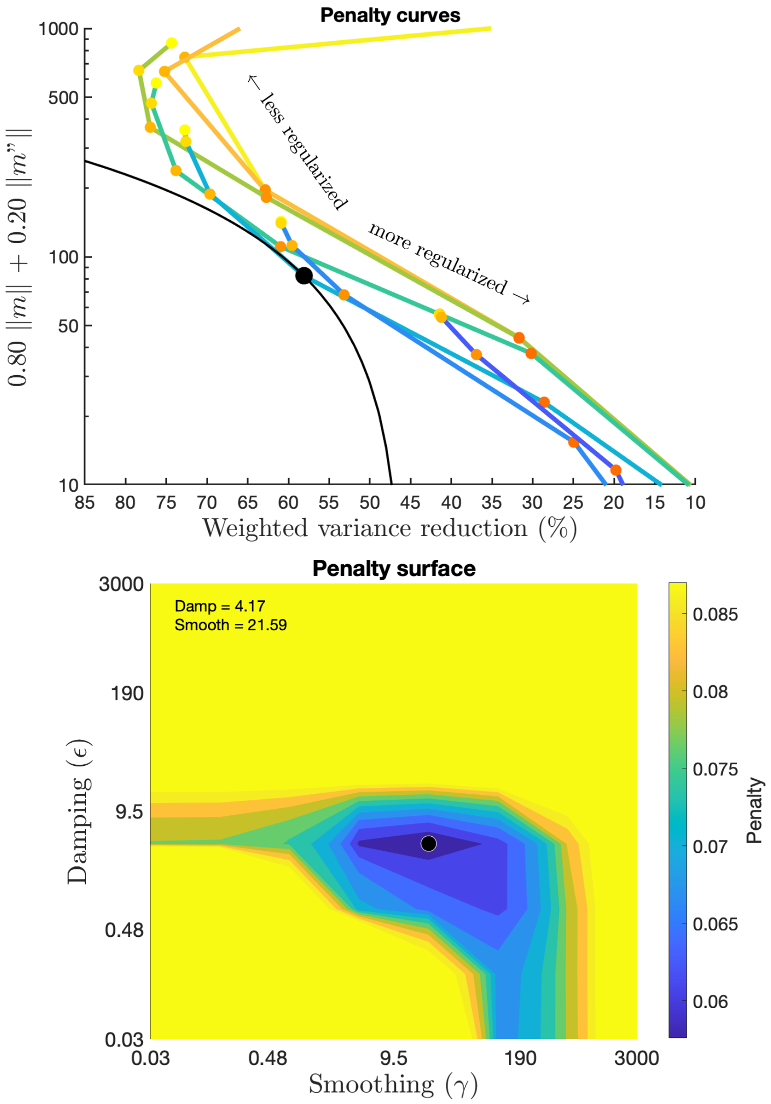

Figure S3. L-test used to determine the appropriate regularization parameters ϵ and γ for damping and second derivative smoothing respectively. The chosen values $\epsilon = 4.2$ and $\gamma = 22$ are plotted as black dots. (Top) Lines of constant γ and varied ϵ, showing linear combination of roughness and norm versus the consequent variance reduction. The black line delineates the maximum trade-off between norm/roughness and variance reduction. (Bottom) Surface showing the penalty (linear combination of model norm, roughness, and residual) associated with each set of ϵ and γ.

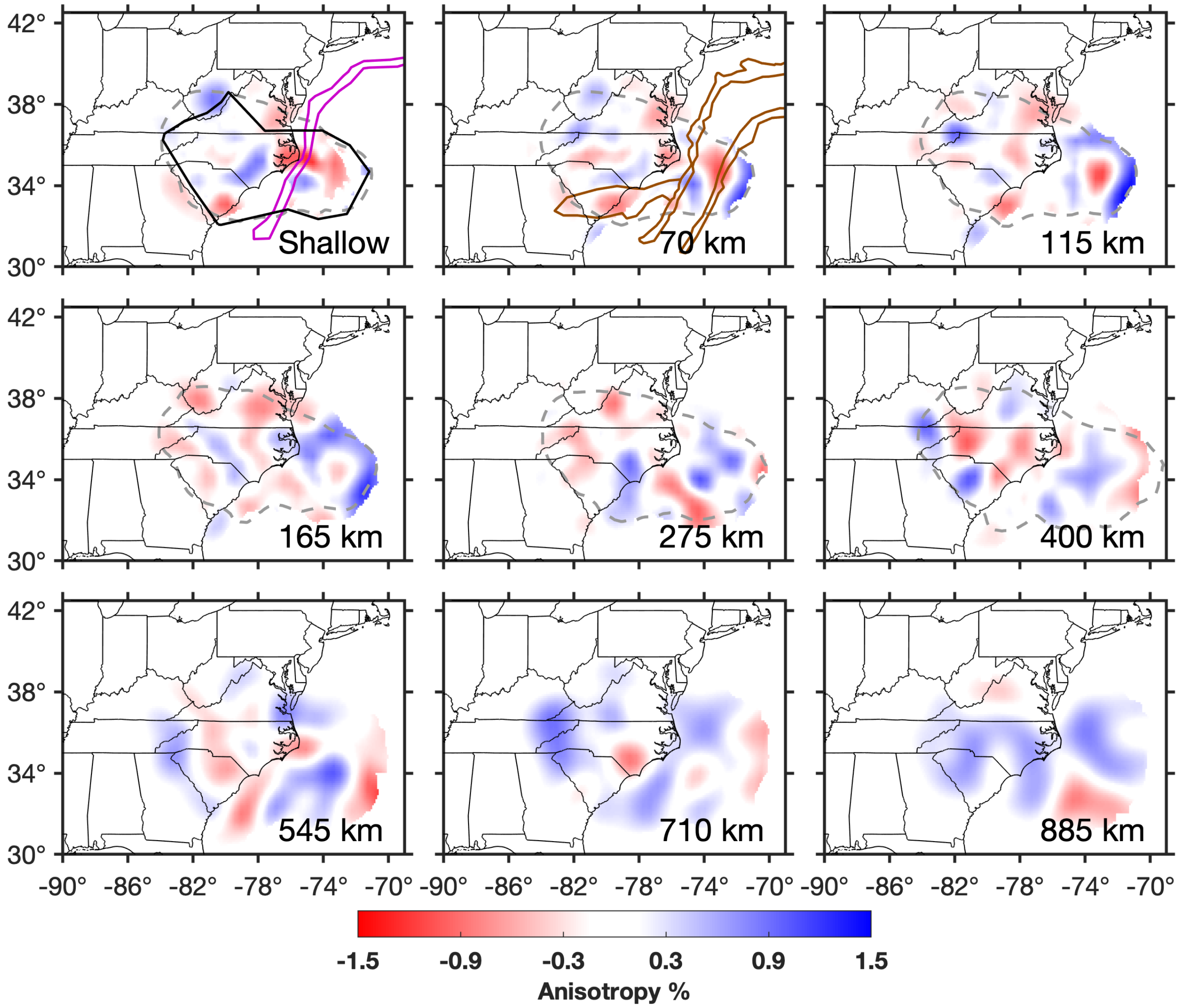

Figure S4. Model where anisotropy was permitted at all depths. See Figure 4 for more description.

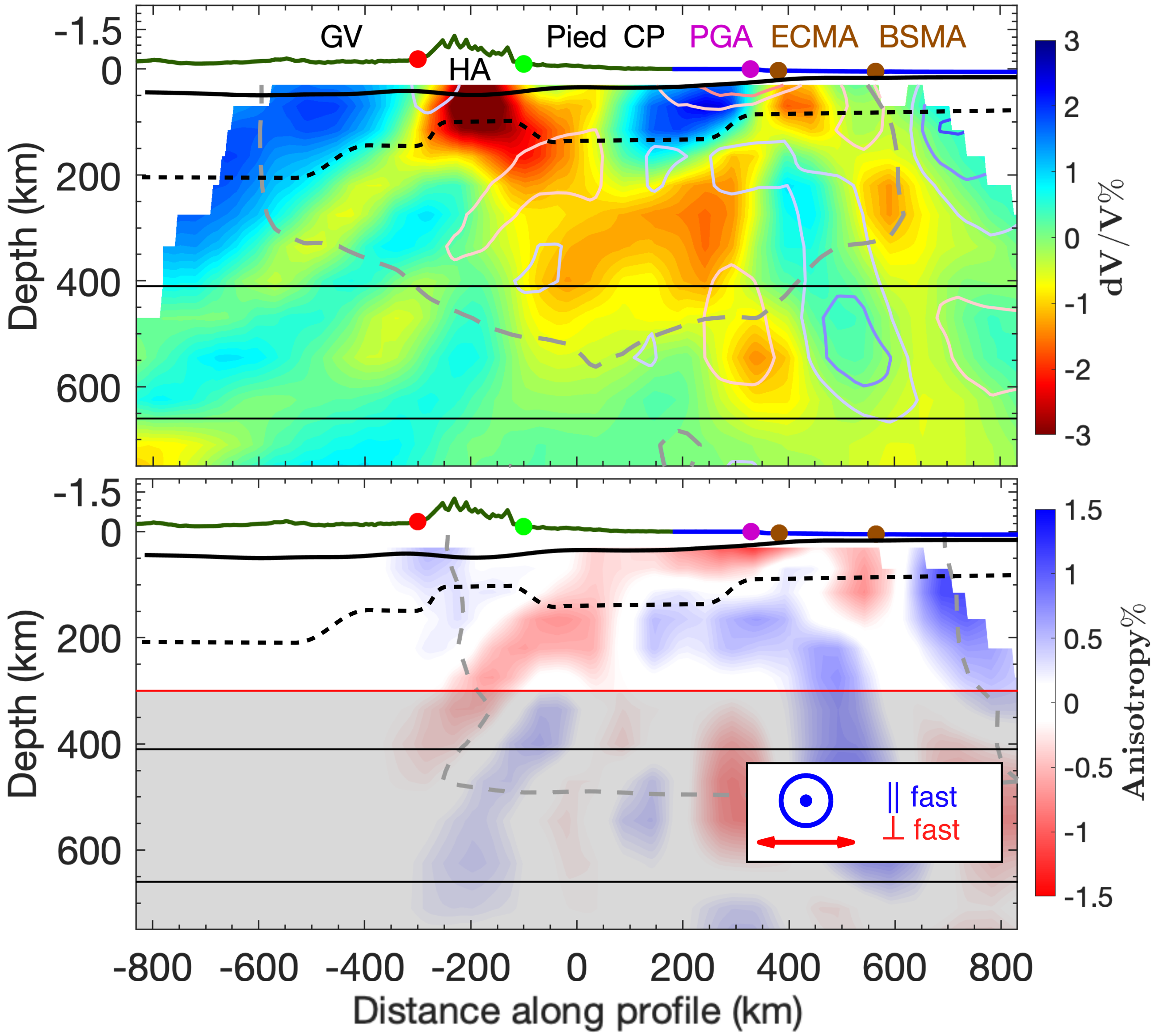

Figure S5. Model where anisotropy was permitted at all depths. See Figure 5 for more description.

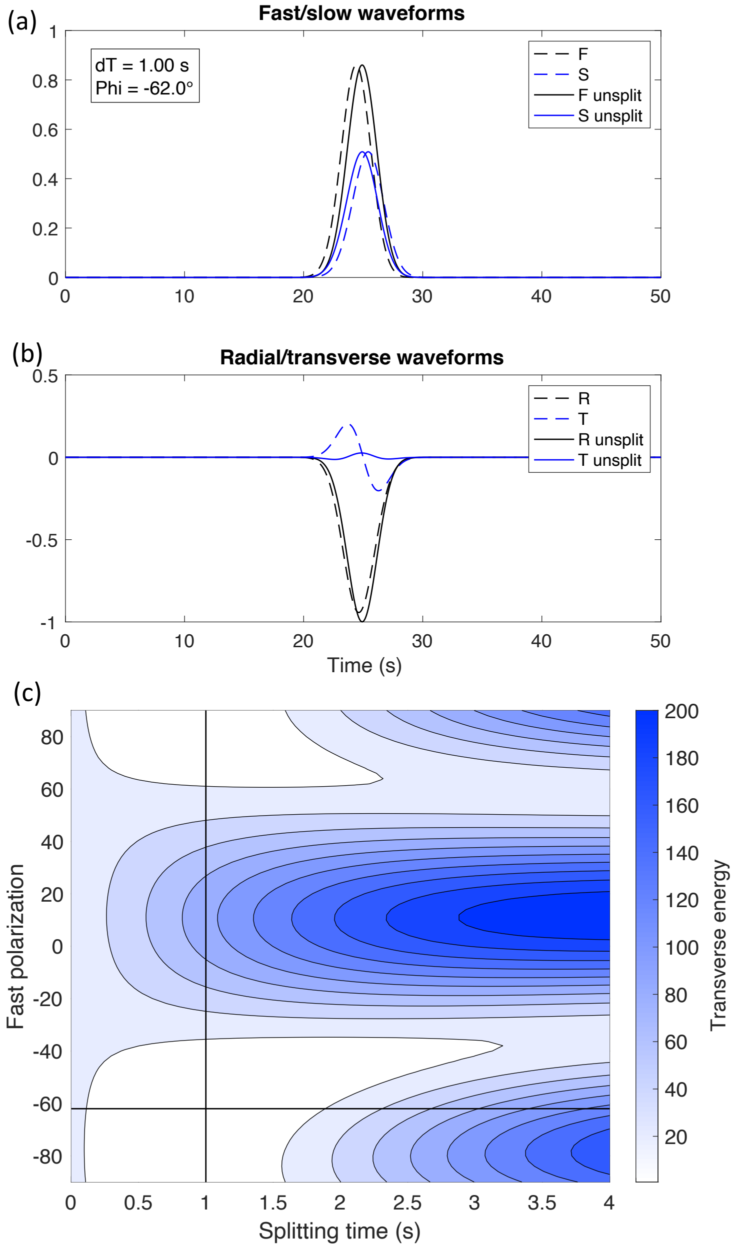

Figure S6. Results of synthetic splitting applied and measured by propagating a Gaussian pulse through the final inverted velocity and anisotropy model. (a) Split and splitting corrected fast (F) and slow (S) polarization components. (b) Split and splitting corrected radial (R) and transverse (T) components. (c) Transverse energy remaining after correcting for splitting. The location of minimum energy, which is plotted with a cross, indicates the splitting time and fast polarization.

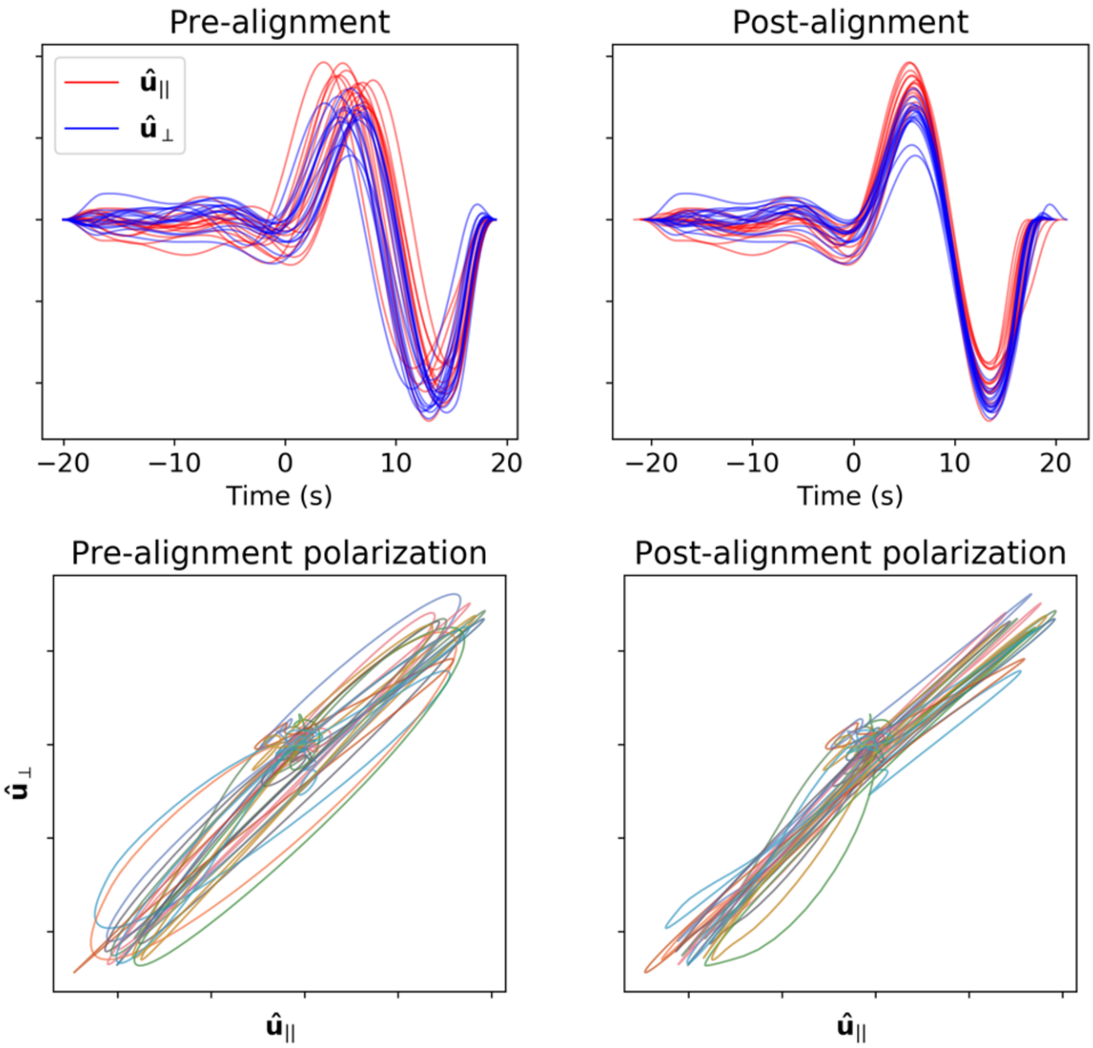

Figure S7. An example of our MCCC results. One earthquake's arrival at several stations are simultaneously plotted. The seismograms are rotated to have one component parallel to the anisotropic symmetry axis, $\mathbf{u}_{||}$, and the other component perpendicular, $\mathbf{u}_\perp$. On the left, the waveforms are aligned by their arrival times predicted from a 1-D velocity model. On the right, results are shifted according to the MCCC inverted differential travel times and splitting times. The top shows waveforms. The bottom shows particle motions, with each color corresponding to a different station. MCCC: Multi-channel cross-correlation.

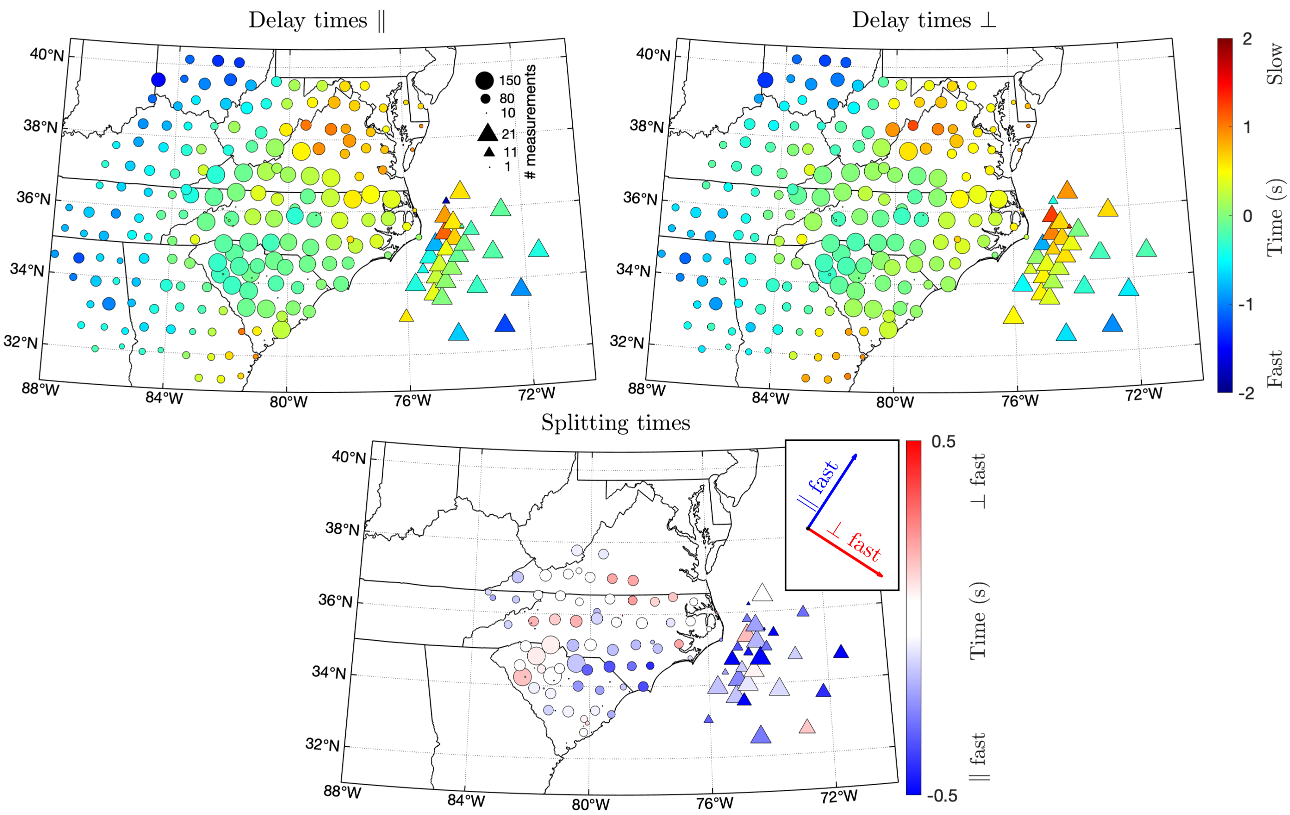

Figure S8. Same as Figure 2, but with results averaged at each station. Times shown are the weighted average of each measurement at a station. The size of a dot represents the number of observations at that station. OBS (plotted as triangles) sizes are multiplied by 8. Sizes are capped between 10 and 150 for clarity. The colorbar for splitting times is capped between −0.5 s and 0.5 s for this figure only.

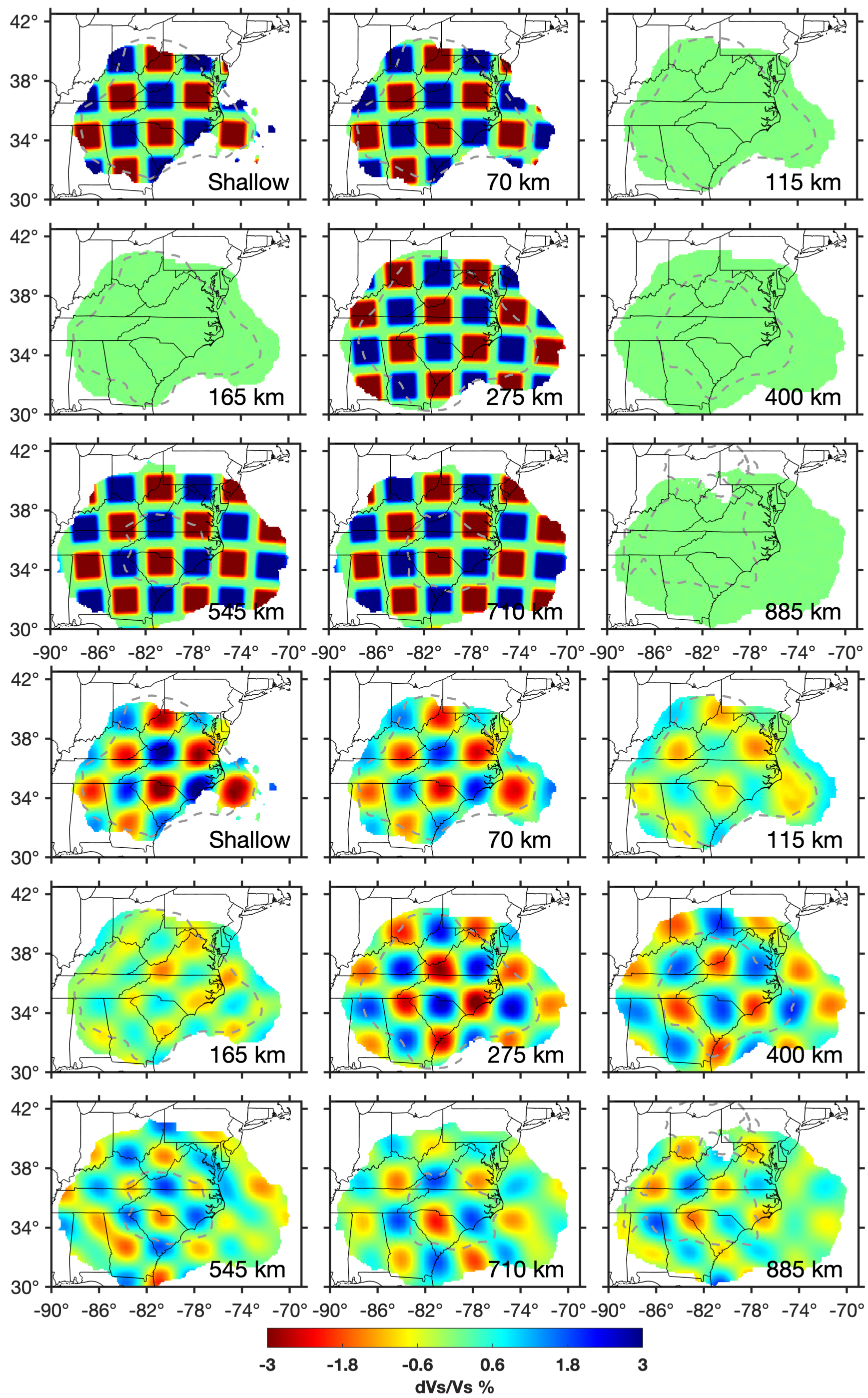

Figure S9. Checkerboard tests for velocity. The top three rows are input and bottom three are output structure. See Figure 3 for more description.

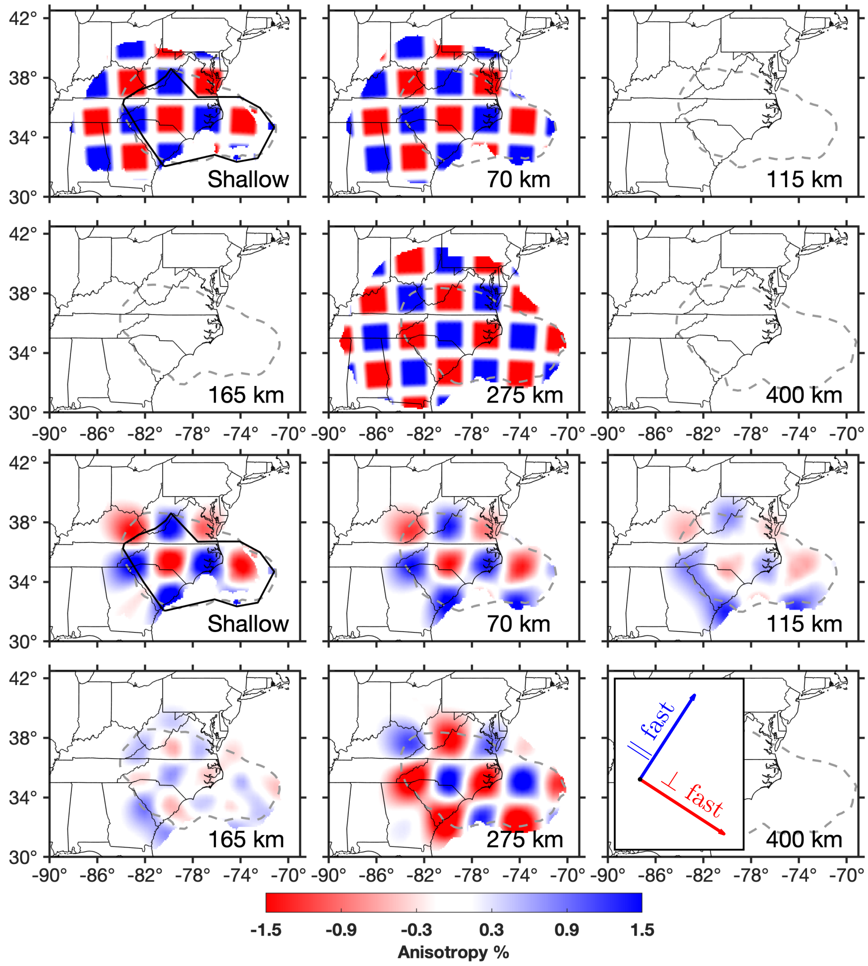

Figure S10. Same as Figure S9, but for anisotropy. See Figure 4 for more description.

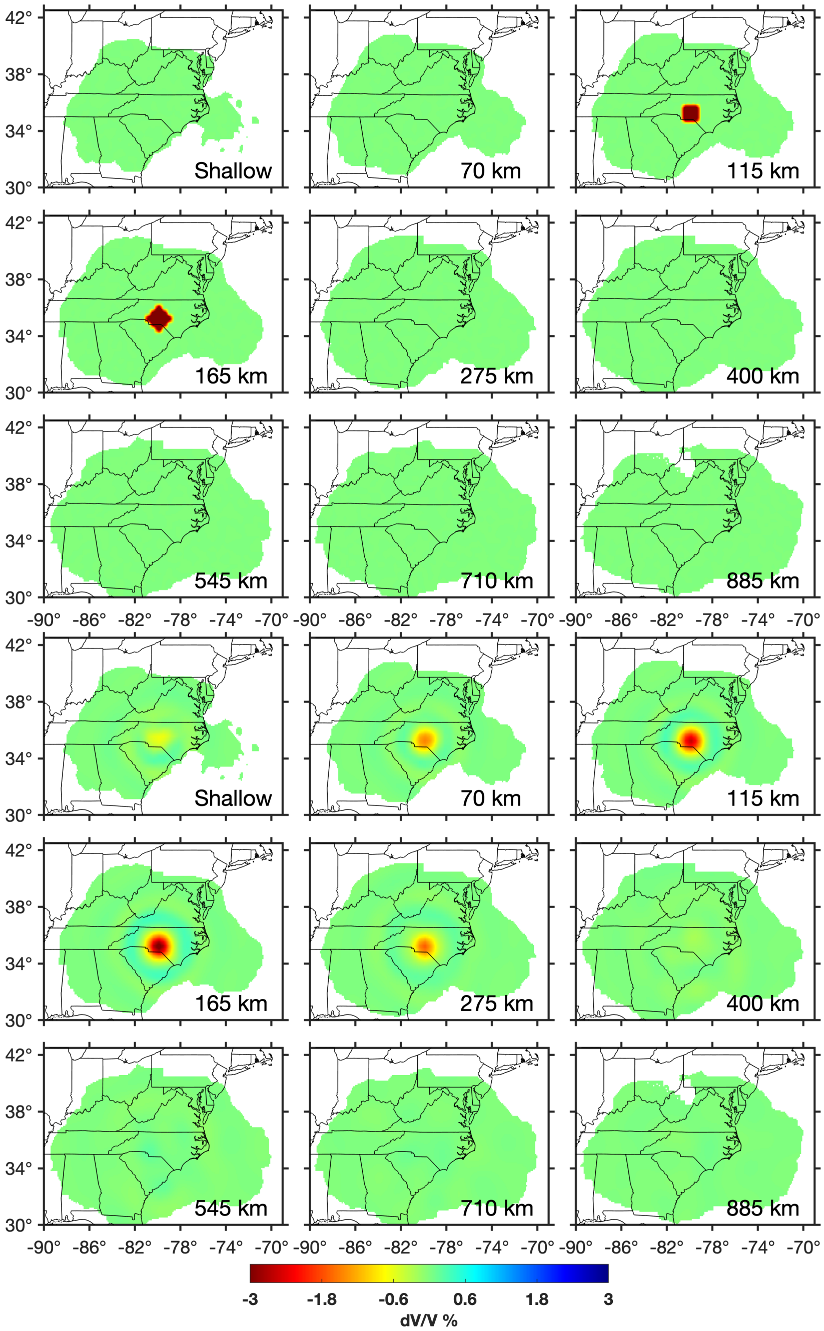

Figure S11. Spike tests using a single spherical spike with a radius of 85 km and center at 165 km depth. Top three rows show input and bottom three rows show output. See Figure 3 for more description.

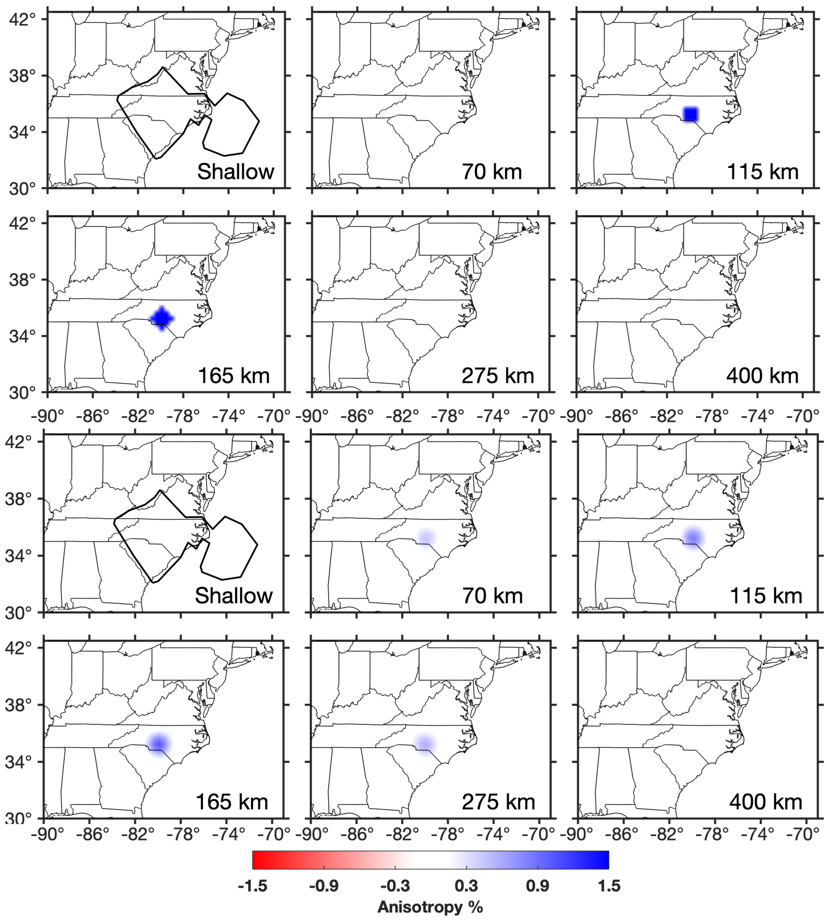

Figure S12. Same as Figure S11, but for anisotropy. Top two rows are input and bottom two rows are output structure. See Figure 4 for more description.

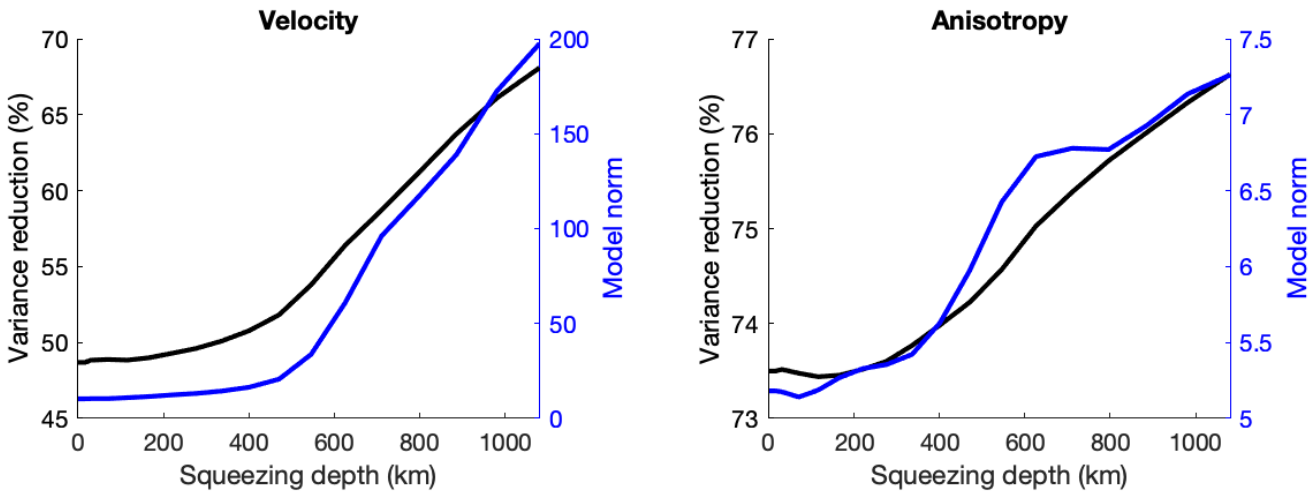

Figure S13. Results of the squeezing test. The squeezing depth z_{sqz} was varied from 0 km to 1080 km. All structure with $z > z_{sqz}$ was assumed to be 0. For each squeezing depth, the resulting model norms for both velocity and anisotropy are shown. The variance reduction of splitting times is shown for the anisotropy figure, while the variance reduction of differential travel times is shown for the velocity figure.

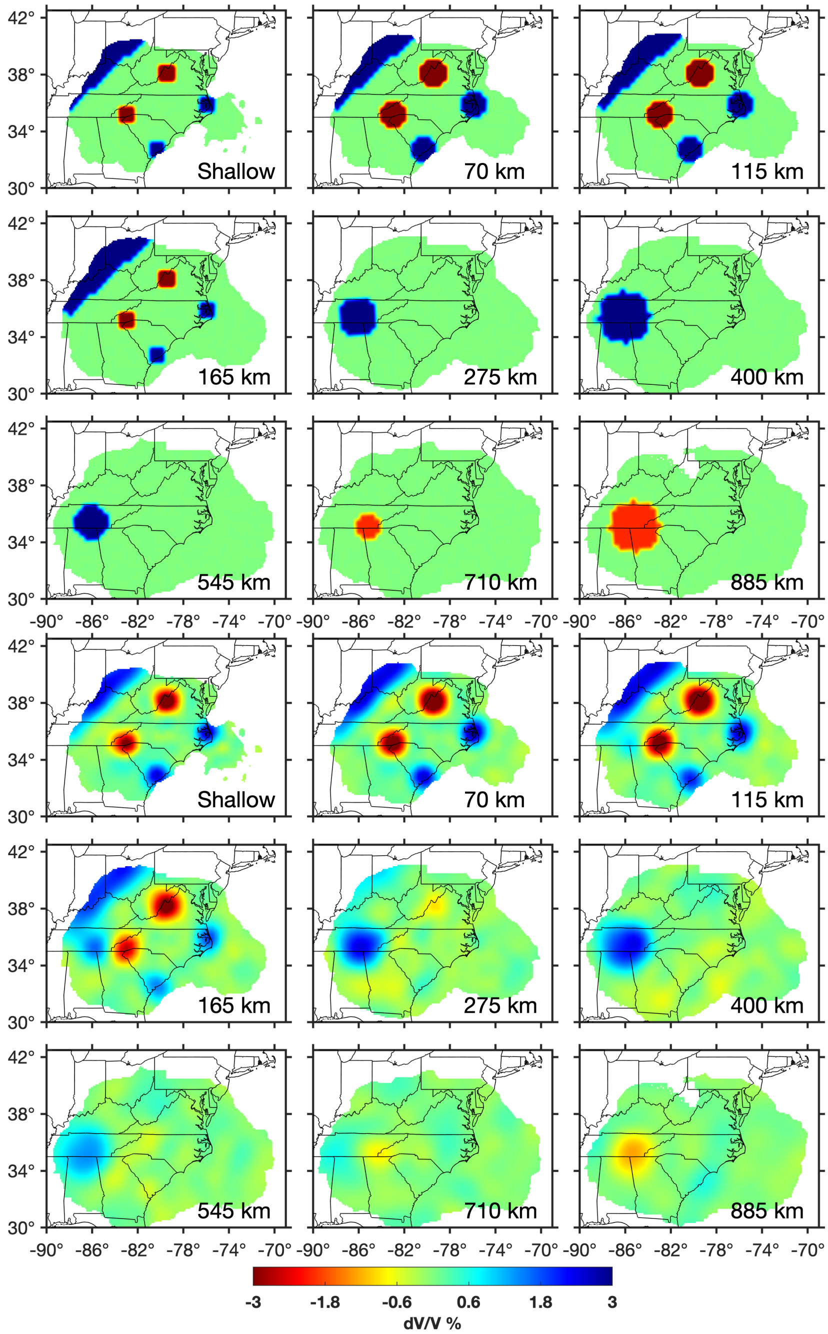

Figure S14. This shows the velocity synthetic input-output tests, where the inputs are chosen to correspond with specific possible observations. Input is top three rows, output is bottom three rows. See Figure 3 for more description.

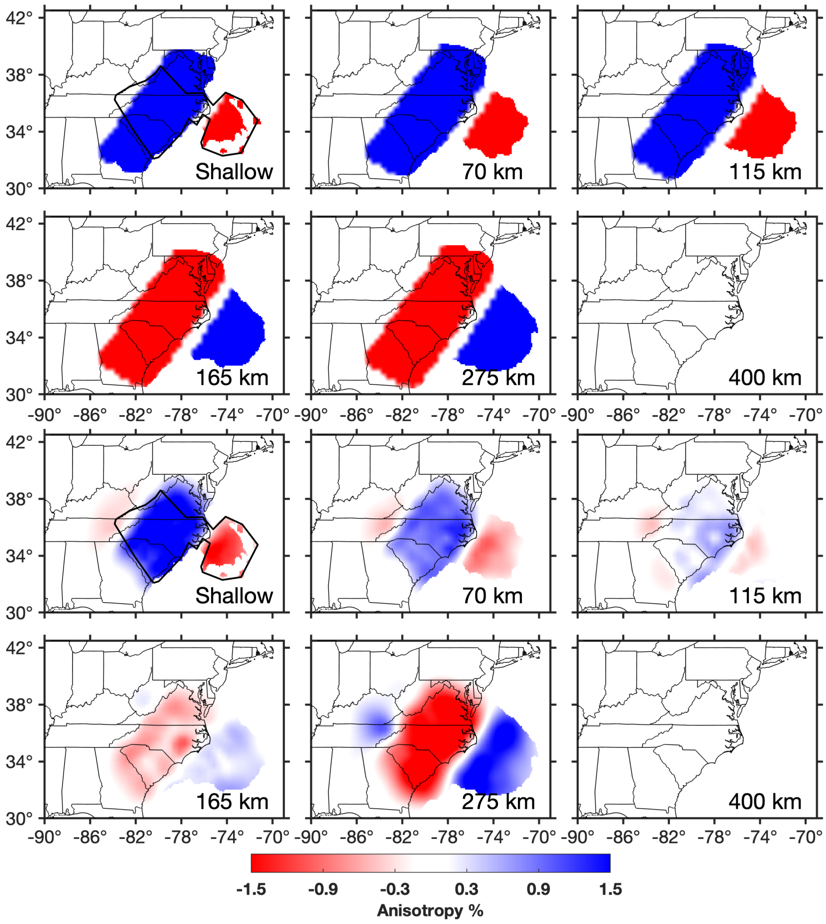

Figure S15. Same as Figure S14, but for anisotropy. See Figure 4 for more description.

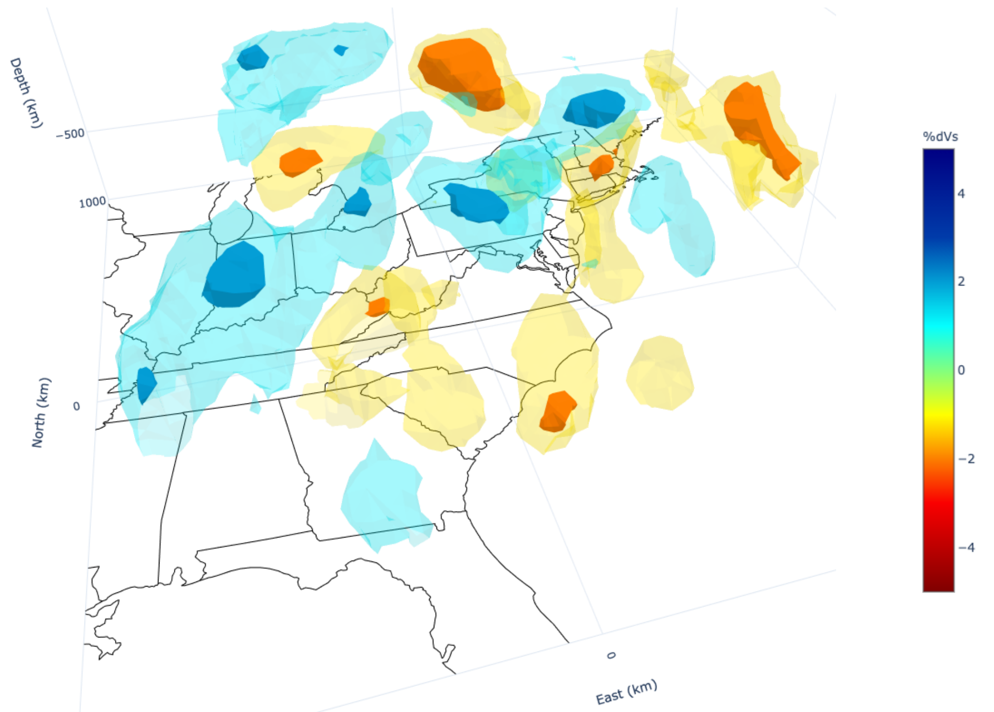

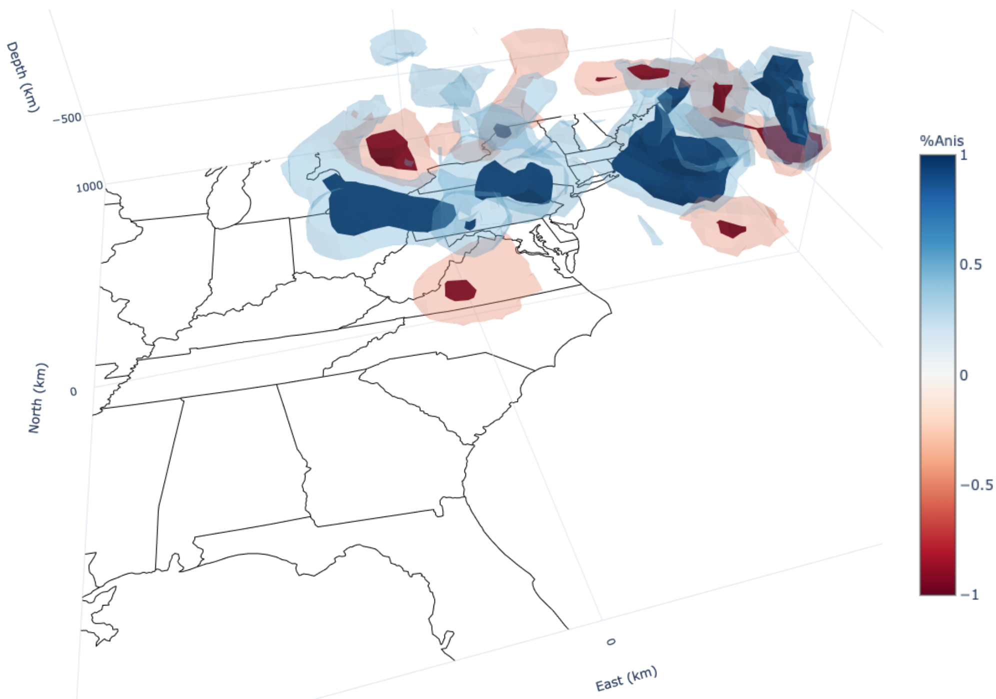

Figure S16. Three-dimensional view of velocity and anisotropy models. dVs isosurfaces are at $\pm1.2\%, \pm2.2\%$. Anisotropy isosurfaces are at $\pm0.5\%, \pm1.0\%$. Model only plotted where hit quality > 0.7. These files can be viewed interactively using the supplementary file `brunsvik-tomog.html`.